Search for single top quark production in $p\bar{p}$ collisions at $\sqrt{s} = 1.96$ TeV in the missing transverse energy plus jets topology

T. Aaltonen,[24] J. Adelman,[14] B. Álvarez González,[12,x] S. Amerio,[44b,44a] D. Amidei,[35] A. Anastassov,[39] A. Annovi,[20] J. Antos,[15] G. Apollinari,[18] J. Appel,[18] A. Apresyan,[49] T. Arisawa,[58] A. Artikov,[16] J. Asaadi,[54] W. Ashmanskas,[18] A. Attal,[4] A. Aurisano,[54] F. Azfar,[43] W. Badgett,[18] A. Barbaro-Galtieri,[29] V. E. Barnes,[49] B. A. Barnett,[26] P. Barria,[47c,47a] P. Bartos,[15] G. Bauer,[33] P.-H. Beauchemin,[34] F. Bedeschi,[47a] D. Beecher,[31] S. Behari,[26] G. Bellettini,[47b,47a] J. Bellinger,[60] D. Benjamin,[17] A. Beretvas,[18] A. Bhatti,[51] M. Binkley,[18] D. Bisello,[44b,44a] I. Bizjak,[31,ee] R. E. Blair,[2] C. Blocker,[7] B. Blumenfeld,[26] A. Bocci,[17] A. Bodek,[50] V. Boisvert,[50] D. Bortoletto,[49] J. Boudreau,[48] A. Boveia,[11] B. Brau,[11,b] A. Bridgeman,[25] L. Brigliadori,[6b,6a] C. Bromberg,[36] E. Brubaker,[14] J. Budagov,[16] H. S. Budd,[50] S. Budd,[25] K. Burkett,[18] G. Busetto,[44b,44a] P. Bussey,[22] A. Buzatu,[34] K. L. Byrum,[2] S. Cabrera,[17,z] C. Calancha,[32] S. Camarda,[4] M. Campanelli,[31] M. Campbell,[35] F. Canelli,[14,18] A. Canepa,[46] B. Carls,[25] D. Carlsmith,[60] R. Carosi,[47a] S. Carrillo,[19,o] S. Carron,[18] B. Casal,[12] M. Casarsa,[18] A. Castro,[6b,6a] P. Catastini,[47c,47a] D. Cauz,[55a] V. Cavaliere,[47c,47a] M. Cavalli-Sforza,[4] A. Cerri,[29] L. Cerrito,[31,r] S. H. Chang,[28] Y. C. Chen,[2] M. Chertok,[8] G. Chiarelli,[47a] G. Chlachidze,[18] F. Chlebana,[18] K. Cho,[28] D. Chokheli,[16] J. P. Chou,[23] K. Chung,[18,p] W. H. Chung,[60] Y. S. Chung,[50] T. Chwalek,[27] C. I. Ciobanu,[45] M. A. Ciocci,[47c,47a] A. Clark,[21] D. Clark,[7] G. Compostella,[44a] M. E. Convery,[18] J. Conway,[8] M. Corbo,[45] M. Cordelli,[20] C. A. Cox,[8] D. J. Cox,[8] F. Crescioli,[47b,47a] C. Cuenca Almenar,[61] J. Cuevas,[12,x] R. Culbertson,[18] J. C. Cully,[35] D. Dagenhart,[18] N. d'Ascenzo,[45,w] M. Datta,[18] T. Davies,[22] P. de Barbaro,[50] S. De Cecco,[52a] A. Deisher,[29] G. De Lorenzo,[4] M. Dell'Orso,[47b,47a] C. Deluca,[4] L. Demortier,[51] J. Deng,[17,g] M. Deninno,[6a] M. d'Errico,[44b,44a] A. Di Canto,[47b,47a] B. Di Ruzza,[47a] J. R. Dittmann,[5] M. D'Onofrio,[4] S. Donati,[47b,47a] P. Dong,[18] T. Dorigo,[44a] S. Dube,[53] K. Ebina,[58] A. Elagin,[54] R. Erbacher,[8] D. Errede,[25] S. Errede,[25] N. Ershaidat,[45,dd] R. Eusebi,[54] H. C. Fang,[29] S. Farrington,[43] W. T. Fedorko,[14] R. G. Feild,[61] M. Feindt,[27] J. P. Fernandez,[32] C. Ferrazza,[47d,47a] R. Field,[19] G. Flanagan,[49,t] R. Forrest,[8] M. J. Frank,[5] M. Franklin,[23] J. C. Freeman,[18] I. Furic,[19] M. Gallinaro,[51] J. Galyardt,[13] F. Garberson,[11] J. E. Garcia,[21] A. F. Garfinkel,[49] P. Garosi,[47c,47a] H. Gerberich,[25] D. Gerdes,[35] A. Gessler,[27] S. Giagu,[52b,52a] V. Giakoumopoulou,[3] P. Giannetti,[47a] K. Gibson,[48] J. L. Gimmell,[50] C. M. Ginsburg,[18] N. Giokaris,[3] M. Giordani,[55b,55a] P. Giromini,[20] M. Giunta,[47a] G. Giurgiu,[26] V. Glagolev,[16] D. Glenzinski,[18] M. Gold,[38] N. Goldschmidt,[19] A. Golossanov,[18] G. Gomez,[12] G. Gomez-Ceballos,[33] M. Goncharov,[33] O. González,[32] I. Gorelov,[38] A. T. Goshaw,[17] K. Goulianos,[51] A. Gresele,[44b,44a] S. Grinstein,[4] C. Grosso-Pilcher,[14] R. C. Group,[18] U. Grundler,[25] J. Guimaraes da Costa,[23] Z. Gunay-Unalan,[36] C. Haber,[29] S. R. Hahn,[18] E. Halkiadakis,[53] B.-Y. Han,[50] J. Y. Han,[50] F. Happacher,[20] K. Hara,[56] D. Hare,[53] M. Hare,[57] R. F. Harr,[59] M. Hartz,[48] K. Hatakeyama,[5] C. Hays,[43] M. Heck,[27] J. Heinrich,[46] M. Herndon,[60] J. Heuser,[27] S. Hewamanage,[5] D. Hidas,[53] C. S. Hill,[11,d] D. Hirschbuehl,[27] A. Hocker,[18] S. Hou,[2] M. Houlden,[30] S.-C. Hsu,[29] R. E. Hughes,[40] M. Hurwitz,[14] U. Husemann,[61] M. Hussein,[36] J. Huston,[36] J. Incandela,[11] G. Introzzi,[47a] M. Iori,[52b,52a] A. Ivanov,[8,q] E. James,[18] D. Jang,[13] B. Jayatilaka,[17] E. J. Jeon,[28] M. K. Jha,[6a] S. Jindariani,[18] W. Johnson,[8] M. Jones,[49] K. K. Joo,[28] S. Y. Jun,[13] J. E. Jung,[28] T. R. Junk,[18] T. Kamon,[54] D. Kar,[19] P. E. Karchin,[59] Y. Kato,[42,n] R. Kephart,[18] W. Ketchum,[14] J. Keung,[46] V. Khotilovich,[54] B. Kilminster,[18] D. H. Kim,[28] H. S. Kim,[28] H. W. Kim,[28] J. E. Kim,[28] M. J. Kim,[20] S. B. Kim,[28] S. H. Kim,[56] Y. K. Kim,[14] N. Kimura,[58] L. Kirsch,[7] S. Klimenko,[19] K. Kondo,[58] D. J. Kong,[28] J. Konigsberg,[19] A. Korytov,[19] A. V. Kotwal,[17] M. Kreps,[27] J. Kroll,[46] D. Krop,[14] N. Krumnack,[5] M. Kruse,[17] V. Krutelyov,[11] T. Kuhr,[27] N. P. Kulkarni,[59] M. Kurata,[56] S. Kwang,[14] A. T. Laasanen,[49] S. Lami,[47a] S. Lammel,[18] M. Lancaster,[31] R. L. Lander,[8] K. Lannon,[40,v] A. Lath,[53] G. Latino,[47c,47a] I. Lazzizzera,[44b,44a] T. LeCompte,[2] E. Lee,[54] H. S. Lee,[14] J. S. Lee,[28] S. W. Lee,[54,y] S. Leone,[47a] J. D. Lewis,[18] C.-J. Lin,[29] J. Linacre,[43] M. Lindgren,[18] E. Lipeles,[46] A. Lister,[21] D. O. Litvintsev,[18] C. Liu,[48] T. Liu,[18] N. S. Lockyer,[46] A. Loginov,[61] L. Lovas,[15] D. Lucchesi,[44b,44a] J. Lueck,[27] P. Lujan,[29] P. Lukens,[18] G. Lungu,[51] J. Lys,[29] R. Lysak,[15] D. MacQueen,[34] R. Madrak,[18] K. Maeshima,[18] K. Makhoul,[33] P. Maksimovic,[26] S. Malde,[43] S. Malik,[31] G. Manca,[30,f] A. Manousakis-Katsikakis,[3] F. Margaroli,[49] C. Marino,[27] C. P. Marino,[25] A. Martin,[61] V. Martin,[22,l] M. Martínez,[4] R. Martínez-Ballarín,[32] P. Mastrandrea,[52a] M. Mathis,[26] M. E. Mattson,[59] P. Mazzanti,[6a] K. S. McFarland,[50] P. McIntyre,[54] R. McNulty,[30,k] A. Mehta,[30] P. Mehtala,[24] A. Menzione,[47a] C. Mesropian,[51] T. Miao,[18] D. Mietlicki,[35] N. Miladinovic,[7] R. Miller,[36] C. Mills,[23] M. Milnik,[27] A. Mitra,[2] G. Mitselmakher,[19] H. Miyake,[56] S. Moed,[23] N. Moggi,[6a] M. N. Mondragon,[18,o] C. S. Moon,[28] R. Moore,[18] M. J. Morello,[47a] J. Morlock,[27] P. Movilla Fernandez,[18] J. Mülmenstädt,[29] A. Mukherjee,[18] Th. Muller,[27] P. Murat,[18] M. Mussini,[6b,6a] J. Nachtman,[18,p] Y. Nagai,[56] J. Naganoma,[56] K. Nakamura,[56] I. Nakano,[41] A. Napier,[57] J. Nett,[60] C. Neu,[46,bb] M. S. Neubauer,[25] S. Neubauer,[27] J. Nielsen,[29,h] L. Nodulman,[2] M. Norman,[10] O. Norniella,[25] E. Nurse,[31] L. Oakes,[43] S. H. Oh,[17] Y. D. Oh,[28] I. Oksuzian,[19] T. Okusawa,[42] R. Orava,[24] K. Osterberg,[24] S. Pagan Griso,[44b,44a]

C. Pagliarone,[55a] E. Palencia,[18] V. Papadimitriou,[18] A. Papaikonomou,[27] A. A. Paramanov,[2] B. Parks,[40] S. Pashapour,[34] J. Patrick,[18] G. Pauletta,[55b,55a] M. Paulini,[13] C. Paus,[33] T. Peiffer,[27] D. E. Pellett,[8] A. Penzo,[55a] T. J. Phillips,[17] G. Piacentino,[47a] E. Pianori,[46] L. Pinera,[19] K. Pitts,[25] C. Plager,[9] L. Pondrom,[60] K. Potamianos,[49] O. Poukhov,[16,a] F. Prokoshin,[16,aa] A. Pronko,[18] F. Ptohos,[18,j] E. Pueschel,[13] G. Punzi,[47b,47a] J. Pursley,[60] J. Rademacker,[43,d] A. Rahaman,[48] V. Ramakrishnan,[60] N. Ranjan,[49] I. Redondo,[32] P. Renton,[43] M. Renz,[27] M. Rescigno,[52a] S. Richter,[27] F. Rimondi,[6b,6a] L. Ristori,[47a] A. Robson,[22] T. Rodrigo,[12] T. Rodriguez,[46] E. Rogers,[25] S. Rolli,[57] R. Roser,[18] M. Rossi,[55a] R. Rossin,[11] P. Roy,[34] A. Ruiz,[12] J. Russ,[13] V. Rusu,[18] B. Rutherford,[18] H. Saarikko,[24] A. Safonov,[54] W. K. Sakumoto,[50] L. Santi,[55b,55a] L. Sartori,[47a] K. Sato,[56] V. Saveliev,[45,w] A. Savoy-Navarro,[45] P. Schlabach,[18] A. Schmidt,[27] E. E. Schmidt,[18] M. A. Schmidt,[14] M. P. Schmidt,[61,a] M. Schmitt,[39] T. Schwarz,[8] L. Scodellaro,[12] A. Scribano,[47c,47a] F. Scuri,[47a] A. Sedov,[49] S. Seidel,[38] Y. Seiya,[42] A. Semenov,[16] L. Sexton-Kennedy,[18] F. Sforza,[47b,47a] A. Sfyrla,[25] S. Z. Shalhout,[59] T. Shears,[30] P. F. Shepard,[48] M. Shimojima,[56,u] S. Shiraishi,[14] M. Shochet,[14] Y. Shon,[60] I. Shreyber,[37] A. Simonenko,[16] P. Sinervo,[34] A. Sisakyan,[16] A. J. Slaughter,[18] J. Slaunwhite,[40] K. Sliwa,[57] J. R. Smith,[8] F. D. Snider,[18] R. Snihur,[34] A. Soha,[18] S. Somalwar,[53] V. Sorin,[4] P. Squillacioti,[47c,47a] M. Stanitzki,[61] R. St. Denis,[22] B. Stelzer,[34] O. Stelzer-Chilton,[34] D. Stentz,[39] J. Strologas,[38] G. L. Strycker,[35] J. S. Suh,[28] A. Sukhanov,[19] I. Suslov,[16] A. Taffard,[25,g] R. Takashima,[41] Y. Takeuchi,[56] R. Tanaka,[41] J. Tang,[14] M. Tecchio,[35] P. K. Teng,[2] J. Thom,[18,i] J. Thome,[13] G. A. Thompson,[25] E. Thomson,[46] P. Tipton,[61] P. Ttito-Guzmán,[32] S. Tkaczyk,[18] D. Toback,[54] S. Tokar,[15] K. Tollefson,[36] T. Tomura,[56] D. Tonelli,[18] S. Torre,[20] D. Torretta,[18] P. Totaro,[55b,55a] M. Trovato,[47d,47a] S.-Y. Tsai,[2] Y. Tu,[46] N. Turini,[47c,47a] F. Ukegawa,[56] S. Uozumi,[28] N. van Remortel,[24,c] A. Varganov,[35] E. Vataga,[47d,47a] F. Vázquez,[19,o] G. Velev,[18] C. Vellidis,[3] M. Vidal,[32] I. Vila,[12] R. Vilar,[12] M. Vogel,[38] I. Volobouev,[29,y] G. Volpi,[47b,47a] P. Wagner,[46] R. G. Wagner,[2] R. L. Wagner,[18] W. Wagner,[27,cc] J. Wagner-Kuhr,[27] T. Wakisaka,[42] R. Wallny,[9] S. M. Wang,[2] A. Warburton,[34] D. Waters,[31] M. Weinberger,[54] J. Weinelt,[27] W. C. Wester III,[18] B. Whitehouse,[57] D. Whiteson,[46,g] A. B. Wicklund,[2] E. Wicklund,[18] S. Wilbur,[14] G. Williams,[34] H. H. Williams,[46] P. Wilson,[18] B. L. Winer,[40] P. Wittich,[18,i] S. Wolbers,[18] C. Wolfe,[14] H. Wolfe,[40] T. Wright,[35] X. Wu,[21] F. Würthwein,[10] A. Yagil,[10] K. Yamamoto,[42] J. Yamaoka,[17] U. K. Yang,[14,s] Y. C. Yang,[28] W. M. Yao,[29] G. P. Yeh,[18] K. Yi,[18,p] J. Yoh,[18] K. Yorita,[58] T. Yoshida,[42,m] G. B. Yu,[17] I. Yu,[28] S. S. Yu,[18] J. C. Yun,[18] A. Zanetti,[55a] Y. Zeng,[17] X. Zhang,[25] Y. Zheng,[9,e] and S. Zucchelli[6b,6a]

(CDF Collaboration)

[2]*Institute of Physics, Academia Sinica, Taipei, Taiwan 11529, Republic of China*
[2]*Argonne National Laboratory, Argonne, Illinois 60439, USA*
[3]*University of Athens, 157 71 Athens, Greece*
[4]*Institut de Fisica d'Altes Energies, Universitat Autonoma de Barcelona, E-08193, Bellaterra (Barcelona), Spain*
[5]*Baylor University, Waco, Texas 76798, USA*
[6a]*Istituto Nazionale di Fisica Nucleare Bologna, I-40127 Bologna, Italy*
[6b]*University of Bologna, I-40127 Bologna, Italy*
[7]*Brandeis University, Waltham, Massachusetts 02254, USA*
[8]*University of California, Davis, Davis, California 95616, USA*
[9]*University of California, Los Angeles, Los Angeles, California 90024, USA*
[10]*University of California, San Diego, La Jolla, California 92093, USA*
[11]*University of California, Santa Barbara, Santa Barbara, California 93106, USA*
[12]*Instituto de Fisica de Cantabria, CSIC-University of Cantabria, 39005 Santander, Spain*
[13]*Carnegie Mellon University, Pittsburgh, Pennsylvania 15213, USA*
[14]*Enrico Fermi Institute, University of Chicago, Chicago, Illinois 60637, USA*
[15]*Comenius University, 842 48 Bratislava, Slovakia; Institute of Experimental Physics, 040 01 Kosice, Slovakia*
[16]*Joint Institute for Nuclear Research, RU-141980 Dubna, Russia*
[17]*Duke University, Durham, North Carolina 27708, USA*
[18]*Fermi National Accelerator Laboratory, Batavia, Illinois 60510, USA*
[19]*University of Florida, Gainesville, Florida 32611, USA*
[20]*Laboratori Nazionali di Frascati, Istituto Nazionale di Fisica Nucleare, I-00044 Frascati, Italy*
[21]*University of Geneva, CH-1211 Geneva 4, Switzerland*
[22]*Glasgow University, Glasgow G12 8QQ, United Kingdom*
[23]*Harvard University, Cambridge, Massachusetts 02138, USA*
[24]*Division of High Energy Physics, Department of Physics, University of Helsinki and Helsinki Institute of Physics, FIN-00014, Helsinki, Finland*
[25]*University of Illinois, Urbana, Illinois 61801, USA*

[26]The Johns Hopkins University, Baltimore, Maryland 21218, USA
[27]Institut für Experimentelle Kernphysik, Karlsruhe Institute of Technology, D-76131 Karlsruhe, Germany
[28]Center for High Energy Physics: Kyungpook National University, Daegu 702-701, Korea;
Seoul National University, Seoul 151-742, Korea;
Sungkyunkwan University, Suwon 440-746, Korea;
Korea Institute of Science and Technology Information, Daejeon 305-806, Korea;
Chonnam National University, Gwangju 500-757, Korea;
Chonbuk National University, Jeonju 561-756, Korea
[29]Ernest Orlando Lawrence Berkeley National Laboratory, Berkeley, California 94720, USA
[30]University of Liverpool, Liverpool L69 7ZE, United Kingdom
[31]University College London, London WC1E 6BT, United Kingdom
[32]Centro de Investigaciones Energeticas Medioambientales y Tecnologicas, E-28040 Madrid, Spain
[33]Massachusetts Institute of Technology, Cambridge, Massachusetts 02139, USA
[34]Institute of Particle Physics: McGill University, Montréal, Québec, Canada H3A 2T8;
Simon Fraser University, Burnaby, British Columbia, Canada V5A 1S6;
University of Toronto, Toronto, Ontario, Canada M5S 1A7;
and TRIUMF, Vancouver, British Columbia, Canada V6T 2A3
[35]University of Michigan, Ann Arbor, Michigan 48109, USA
[36]Michigan State University, East Lansing, Michigan 48824, USA
[37]Institution for Theoretical and Experimental Physics, ITEP, Moscow 117259, Russia
[38]University of New Mexico, Albuquerque, New Mexico 87131, USA
[39]Northwestern University, Evanston, Illinois 60208, USA
[40]The Ohio State University, Columbus, Ohio 43210, USA
[41]Okayama University, Okayama 700-8530, Japan
[42]Osaka City University, Osaka 588, Japan
[43]University of Oxford, Oxford OX1 3RH, United Kingdom
[44a]Istituto Nazionale di Fisica Nucleare, Sezione di Padova-Trento, I-35131 Padova, Italy
[44b]University of Padova, I-35131 Padova, Italy
[45]LPNHE, Universite Pierre et Marie Curie/IN2P3-CNRS, UMR7585, Paris, F-75252 France
[46]University of Pennsylvania, Philadelphia, Pennsylvania 19104, USA
[47a]Istituto Nazionale di Fisica Nucleare Pisa, I-56127 Pisa, Italy
[47b]University of Pisa, I-56127 Pisa, Italy
[47c]University of Siena, I-56127 Pisa, Italy

[a]Deceased.
[b]Visitor from University of Massachusetts Amherst, Amherst, MA 01003, USA.
[c]Visitor from Universiteit Antwerpen, B-2610 Antwerp, Belgium.
[d]Visitor from University of Bristol, Bristol BS8 1TL, United Kingdom.
[e]Visitor from Chinese Academy of Sciences, Beijing 100864, China.
[f]Visitor from Istituto Nazionale di Fisica Nucleare, Sezione di Cagliari, 09042 Monserrato (Cagliari), Italy.
[g]Visitor from University of California Irvine, Irvine, CA 92697, USA.
[h]Visitor from University of California Santa Cruz, Santa Cruz, CA 95064, USA.
[i]Visitor from Cornell University, Ithaca, NY 14853, USA.
[j]Visitor from University of Cyprus, Nicosia CY-1678, Cyprus.
[k]Visitor from University College Dublin, Dublin 4, Ireland.
[l]Visitor from University of Edinburgh, Edinburgh EH9 3JZ, United Kingdom.
[m]Visitor from University of Fukui, Fukui City, Fukui Prefecture, Japan 910-0017.
[n]Visitor from Kinki University, Higashi-Osaka City, Japan 577-8502.
[o]Visitor from Universidad Iberoamericana, Mexico D.F., Mexico.
[p]Visitor from University of Iowa, Iowa City, IA 52242, USA.
[q]Visitor from Kansas State University, Manhattan, KS 66506, USA.
[r]Visitor from Queen Mary, University of London, London, E1 4NS, England, United Kingdom.
[s]Visitor from University of Manchester, Manchester M13 9PL, England, United Kingdom.
[t]Visitor from Muons, Inc., Batavia, IL 60510, USA.
[u]Visitor from Nagasaki Institute of Applied Science, Nagasaki, Japan.
[v]Visitor from University of Notre Dame, Notre Dame, IN 46556, USA.
[w]Visitor from Obninsk State University, Obninsk, Russia.
[x]Visitor from University de Oviedo, E-33007 Oviedo, Spain.
[y]Visitor from Texas Tech University, Lubbock, TX 79609, USA.
[z]Visitor from IFIC (CSIC-Universitat de Valencia), 56071 Valencia, Spain.
[aa]Visitor from Universidad Tecnica Federico Santa Maria, 110v Valparaiso, Chile.
[bb]Visitor from University of Virginia, Charlottesville, VA 22906, USA.
[cc]Visitor from Bergische Universität Wuppertal, 42097 Wuppertal, Germany.
[dd]Visitor from Yarmouk University, Irbid 211-63, Jordan.
[ee]On leave from J. Stefan Institute, Ljubljana, Slovenia.

[47d]*Scuola Normale Superiore, I-56127 Pisa, Italy*
[48]*University of Pittsburgh, Pittsburgh, Pennsylvania 15260, USA*
[49]*Purdue University, West Lafayette, Indiana 47907, USA*
[50]*University of Rochester, Rochester, New York 14627, USA*
[51]*The Rockefeller University, New York, New York 10021, USA*
[52a]*Istituto Nazionale di Fisica Nucleare, Sezione di Roma 1, I-00185 Roma, Italy*
[52b]*Sapienza Università di Roma, I-00185 Roma, Italy*
[53]*Rutgers University, Piscataway, New Jersey 08855, USA*
[54]*Texas A&M University, College Station, Texas 77843, USA*
[55a]*Istituto Nazionale di Fisica Nucleare Trieste/Udine, I-34100 Trieste, Italy*
[55b]*University of Trieste/Udine, I-33100 Udine, Italy*
[56]*University of Tsukuba, Tsukuba, Ibaraki 305, Japan*
[57]*Tufts University, Medford, Massachusetts 02155, USA*
[58]*Waseda University, Tokyo 169, Japan*
[59]*Wayne State University, Detroit, Michigan 48201, USA*
[60]*University of Wisconsin, Madison, Wisconsin 53706, USA*
[61]*Yale University, New Haven, Connecticut 06520, USA*
(Received 10 February 2010; published 20 April 2010)

We report a search for single top quark production with the CDF II detector using 2.1 fb^{-1} of integrated luminosity of $p\bar{p}$ collisions at $\sqrt{s} = 1.96$ TeV. The data selected consist of events characterized by large energy imbalance in the transverse plane and hadronic jets, and no identified electrons and muons, so the sample is enriched in $W \to \tau\nu$ decays. In order to suppress backgrounds, additional kinematic and topological requirements are imposed through a neural network, and at least one of the jets must be identified as a b quark jet. We measure an excess of signal-like events in agreement with the standard model prediction, but inconsistent with a model without single top quark production by 2.1 standard deviations (σ), with a median expected sensitivity of 1.4σ. Assuming a top quark mass of 175 GeV/c^2 and ascribing the excess to single top quark production, the cross section is measured to be $4.9^{+2.5}_{-2.2}$(stat + syst) pb, consistent with measurements performed in independent data sets and with the standard model prediction.

DOI: 10.1103/PhysRevD.81.072003 PACS numbers: 12.15.Hh, 13.85.Ni, 14.65.Ha

I. INTRODUCTION

At the Tevatron the dominant standard model (SM) mechanism for top quark production in $p\bar{p}$ collisions is the production through strong interactions of $t\bar{t}$ pairs with a cross section of approximately 7.0 pb [1]. Top quarks can also be produced singly through electroweak processes, which are interesting in their own right. The single top quark production cross section is directly proportional to the square of the magnitude of the $|V_{tb}|$ element of the Cabibbo-Kobayashi-Maskawa (CKM) matrix [2,3]. A measurement of the single top quark production cross section thus constrains the value of the latter. A value of $|V_{tb}|$ smaller than unity could thus indicate the presence of a fourth family of quarks [4], while on the other hand an apparent $|V_{tb}|$ value significantly greater than 1 could point, for instance, to the existence of a heavy W-like boson enhancing the cross section. A review of new physics models affecting the single top quark production cross section is given in Ref. [5].

At the Tevatron, a single top quark can be produced at leading order (LO) together with a b quark in the s channel, or paired with a light quark in the t channel (the charge conjugated process is assumed throughout). The t-channel process also has a large next-to-leading-order (NLO) contribution which gives an additional $\bar{b}$ quark in the final state. The Feynman diagrams for the above processes are shown in Fig. 1. The SM NLO calculations predict the single top quark production cross section to be $\sigma_s = 0.88 \pm 0.11$ pb for the s channel and $\sigma_t = 1.98 \pm 0.25$ pb for the t channel [6–8], for an assumed top quark mass of 175 GeV/c^2.

The top quark has a predicted lifetime of roughly 10^{-25} s, and the SM predicts it decays into a W boson and a b quark almost 100% of the time, assuming $|V_{tb}|^2 \gg |V_{ts}|^2 + |V_{td}|^2$. The W boson subsequently decays to either a quark-antiquark pair or a lepton pair. Events with decays $W \to e\nu$ and $W \to \mu\nu$ are the favored identification modes at a hadron collider due to the presence of the charged lepton and large missing transverse energy from the neutrino. This signature has also acceptance to $W \to \tau\nu$ decays in which the tau decays to e or μ. The identification of the charged lepton and the missing transverse energy suppresses the otherwise large QCD background. Electroweak production of top quarks is difficult to isolate due to the low cross section and large backgrounds which can be estimated only with large uncertainties on their rates.

The first evidence of electroweak top quark production has been achieved by the D0 Collaboration with the

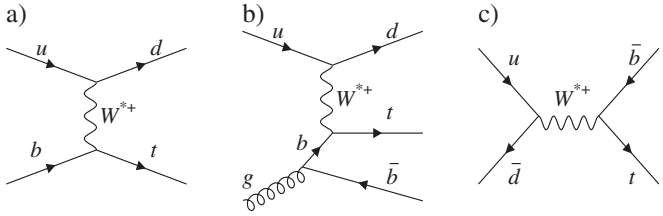

FIG. 1. Feynman diagrams for single top quark production. Represented are the LO (a) and NLO (b) t-channel processes, and the LO s-channel process (c).

charged lepton plus missing energy plus jets signature using 0.9 fb^{-1} of integrated luminosity [9,10]. A more recent measurement in the same decay mode with an observed significance of 3.7σ has been released by the CDF Collaboration using 2.2 fb^{-1} of integrated luminosity [11]. In March 2009, both collaborations achieved the observation (5.0σ significance) level, using 2.3 fb^{-1} and up to 3.2 fb^{-1} of integrated luminosity for the D0 Collaboration [12] and the CDF Collaboration [13], respectively.

To add acceptance to the data set with identified e or μ, the CDF observation paper [13] uses for the first time events containing jets, large missing transverse energy, and no reconstructed electrons or muons. The analysis of these events is described in this paper. This signature comprises events with $W \rightarrow \tau\nu$ decays where the hadronic τ decays are dominant, and with $W \rightarrow e\nu$ or $W \rightarrow \mu\nu$ decays where the e, μ are unidentified. Because the event selection vetoes on the presence of a reconstructed e or μ this measurement is statistically independent from the one in Ref. [11]. The single top quark candidate events analyzed share the same signature as events where the SM Higgs boson is produced in association with a W or Z boson, where the W decays leptonically in either hadronic τ's or unidentified e or μ, or the Z decays to neutrinos. The techniques used in this single top quark search are shared with the ones deployed in the SM Higgs boson search in the same signature [14]. Since the single top quark events are a background to the SM Higgs boson search, measuring the single top quark production cross section in this sample means getting a step closer to reaching sensitivity to the SM Higgs boson signal.

With respect to the single top quark search in the sample with identified leptons [11] this analysis has the extra challenge of much larger backgrounds masking the presence of the signal. In fact, the sample under study is dominated by QCD multijet production, where a mismeasurement of one or more of the jet energies yields large energy imbalance in the detector. The QCD background dominates the signal by 4 orders of magnitude after the application of the online trigger selection. Also, the absence of reconstructed charged leptons and the presence of the neutrino result in underconstrained kinematics, leaving us with the impossibility to reconstruct the top quark invariant mass from its decay products. To improve the signal-to-background ratio (s/b), we select jets identified as originating from b quarks using b-tagging algorithms. Even after these requirements, the s/b is still too low to achieve sensitivity to single top quark production. We further exploit the kinematic and topological characteristics of single top quark events using neural networks to isolate the signal from the dominant QCD background and subsequently from the remaining backgrounds.

We report results based on data taken with the CDF II detector between July 2002 and August 2007, corresponding to an integrated luminosity of 2.1 fb^{-1}. The paper is organized as follows. Section II contains a brief description of the CDF II detector. The analyzed data set is described in Sec. III. Section IV contains the definition of the reconstructed objects used in this analysis. In Sec. V we discuss the Monte Carlo simulation and data-based techniques we use to model the signal and the backgrounds. Section VI describes the preselection and the neural network event selection used to suppress the dominant QCD background. Section VII describes the distribution used to scan for a signal, while Sec. VIII lists the sources of systematic uncertainties that affect the final result. Section IX presents the likelihood procedure used to measure the cross section and the $|V_{tb}|$ matrix element. The single top quark production cross section measured in missing transverse energy plus jets events is presented in Sec. X. Finally, results are summarized in Sec. XI.

II. THE CDF II DETECTOR

The CDF II detector [15] is an azimuthally and forward-backward symmetric apparatus designed to study $p\bar{p}$ collisions at the Fermilab Tevatron. It uses a cylindrical coordinate system as described in [16]. It consists of a magnetic spectrometer surrounded by calorimeters and muon detectors. The charged particle tracking system is contained in a 1.4 T solenoid in which the magnetic field is parallel to the beam. A set of silicon microstrip detectors provides charged particle tracking in the radial distance from 1.5 to 28 cm [17–19]. A 3.1 m long open-cell drift chamber, the central outer tracker (COT) [20], covers the radial distance from 40 to 137 cm. The COT provides up to 96 measurements of the track position with alternating axial and $\pm 2°$-stereo superlayers of 12-wire layers each. The fiducial region of the silicon detector extends in pseudorapidity $|\eta|$ up to $|\eta| \leq 2$, while the COT provides full radial coverage up to $|\eta| \leq 1$. Segmented electromagnetic and hadronic calorimeters surround the tracking system and measure the energy of interacting particles.

The electromagnetic and hadronic calorimeters are lead-scintillator and iron-scintillator sampling devices, respectively, covering the range $|\eta| \leq 3.6$. They are segmented in the central region ($|\eta| < 1.1$) in towers of 0.1 in η and 15° in azimuthal angle ϕ, and in the forward region ($1.1 < |\eta| < 3.6$) in towers of 0.1 to 0.64 units of η (correspond-

ing to a nearly constant 2.7° change in polar angle) and 7.5° in azimuthal angle for $1.1 < |\eta| < 2.11$ and 15° for $|\eta| > 2.11$. The electromagnetic calorimeters [21,22] are instrumented with proportional and scintillating strip detectors that measure the transverse profile of electromagnetic showers at a depth corresponding to the expected shower maximum. The measured energy resolution for electrons in the electromagnetic calorimeters are $13.5\%/\sqrt{E_T} \oplus 2\%$ in the central region, and $16\%/\sqrt{E_T} \oplus 1\%$ in the forward region [23] where the units of E_T are in GeV. We also measure the single-particle (pion) energy resolution in the hadronic calorimeters to be $50\%/\sqrt{E_T} \oplus 3\%$ for the central and $80\%/\sqrt{E_T} \oplus 5\%$, for the forward detector [24].

Drift chambers located outside the central hadronic calorimeters and behind a 60 cm thick iron shield detect muons with $|\eta| \leq 0.6$ [25]. Additional drift chambers and scintillation counters detect muons in the region $0.6 < |\eta| < 1.5$ [26]. Gas Cherenkov counters with a coverage of $3.7 < |\eta| < 4.7$ measure the average number of inelastic $p\bar{p}$ collisions and thereby determine the luminosity [27].

III. $\not\!\!E_T$ PLUS JETS DATA SET

The events of interest are those with a top quark produced in association with one or more jets, where the top quark decays to a b quark and a W boson, and the W boson decays leptonically. Since we are looking at events with nonidentified electrons and muons, or hadronically decaying taus, we use a trigger devised to select events on the presence of two calorimetric jets and large missing transverse energy. The missing transverse energy $\vec{\not\!\!E}_T$ is calculated as the negative vector sum of the energy in each calorimeter tower multiplied by a unit vector in the azimuthal direction of the tower. The $\not\!\!E_T$ symbol is used for the magnitude of $\vec{\not\!\!E}_T$.

CDF uses a three-level trigger system, the first two consisting of special purpose electronics and the third level consisting of conventional computer processors. For triggering purposes the calorimeter granularity is simplified to a 24×24 grid in $\eta - \phi$ space and each trigger tower spans approximately 15° in ϕ and 0.2 in η covering one or two physical towers. At level 1, $\not\!\!E_T \geq 25$ GeV is required, while at level 2 we require the presence of two calorimetric clusters, each with transverse energy greater than 10 GeV. Finally, at level 3 $\not\!\!E_T \geq 35$ GeV is required. With increasing instantaneous luminosity delivered by the Tevatron collider, tighter constraints at trigger level were needed. Starting from March 2005, the level 2 trigger definition changed by demanding that one of the two calorimeter energy clusters be central, i.e. $|\eta| \leq 1.1$. The steadily increasing Tevatron performance required an additional change in November 2006, where the trigger path was turned off as soon as the initial luminosity exceeded 1.90×10^{32} cm^{-2} s^{-1}. Starting from April 2007, for instantaneous luminosity above 2×10^{32} cm^{-2} s^{-1} events were randomly discarded based on a scaling factor between 1 and 40 to keep the trigger rate at a reasonable level.

Overall, 14 963 805 events pass the online trigger requirements, corresponding to an average effective cross section for the data collected by the trigger around 10 nb. The single top quark production cross section times $W \to \ell\nu$ branching ratio is about 1 pb, further reduced by the fact that this analysis is devised to collect mostly $W \to \tau\nu$ decays and only a fraction of the $W \to e/\mu\nu$ decays. The s/b ratio for events surviving the trigger level selection is thus of the order of $1/10\,000$.

The $\not\!\!E_T$ plus jets trigger efficiency is computed using data collected with a high p_T muon, and with data collected with a trigger requiring the presence of a jet with $E_T > 20$ GeV. Trigger efficiencies are calculated for all three levels of the CDF trigger, and are then parametrized as a function of $\not\!\!E_T$ and E_T of the jets. The systematic uncertainties originating from the choice of the samples used in the efficiency calculations are large at small $\not\!\!E_T$, and therefore we require every event to have $\not\!\!E_T > 50$ GeV. The trigger is nearly 100% efficient if the jets with the highest and second highest transverse energies satisfy the conditions $E_T^{j_1} > 35$ GeV and $E_T^{j_2} > 25$ GeV, respectively. Additionally, we require the spatial separation between the two leading E_T jets to be greater than $\Delta R = 1$, where $\Delta R = \sqrt{\Delta\eta^2 + \Delta\phi^2}$ is the distance in the $\eta - \phi$ space between the two jet centroids, in order to avoid jet merging performed by the level 2 jet clustering algorithm. A small fraction of events do not pass the level 1 requirements due to a hardware problem, and are recovered with a trigger on inclusive jets [28].

IV. EVENT RECONSTRUCTION

Events are considered whenever the primary event vertex is reconstructed inside the luminous region ($|z| <$ 60 cm) along the beam axis. Jets are identified using a fixed-cone algorithm which loops over calorimetric towers, with a cone radius of 0.4 in $\eta - \phi$ space. The jet energies are corrected for variations in calorimeter response and the presence of multiple $p\bar{p}$ collisions. First, we take into account calorimeter response variations in η and over time, and energy loss in the uninstrumented regions. After a small correction for the extra energy deposited inside the jet cone by multiple collisions in the same accelerator bunch crossing, a correction for calorimeter nonlinearity is applied so that the jet energies correspond to the most probable in-cone hadronic energy. Each of these steps has an individual systematic uncertainty that is added in quadrature to derive the total uncertainty which decreases from 8% for jet transverse energies around 15 GeV down to 3% for jet energies above 60 GeV.

After these corrections the jet energy provides a good estimate of the initial parton energy. This is verified by transverse momentum balance in events with a single jet

recoiling against a well-measured probe object such as a prompt photon or a $Z \to \ell^+\ell^-$ [29]. Jet energies are further corrected using the algorithm developed by the H1 Collaboration [30], which combines the measurement of the momentum of charged particles in the spectrometer with the calorimeter energy measurement.

In order to improve the s/b ratio, we exploit the heavy-flavor content of single top quark events using a b-tagging algorithm based on secondary vertex reconstruction (SECVTX) as described in detail in Ref. [31]. The algorithm aims at the identification of jets containing a b hadron by reconstructing its decay vertex with at least two good quality tracks with hits in the silicon vertex detector. A b-tagged jet must have a secondary vertex displaced from the primary vertex by more than $7.5\sigma_{\mathrm{VTX}}$ in the transverse plane, where $\sigma_{\mathrm{VTX}} = 190\ \mu$m is the typical secondary vertex spacial resolution in the transverse plane. A second algorithm, JETPROB, is also used to identify jets originating from b quarks. This algorithm computes the probability that all tracks associated with a jet come from the primary $p\bar{p}$ interaction vertex. The probability calculation is based on the impact parameters of the tracks in the jet, and their uncertainties [32]. We consider a jet to be JETPROB tagged when the probability of all jet tracks to come from the primary vertex is less than 0.05. Electrons are reconstructed as charged particles in the tracking system that leave the majority of their energy in the electromagnetic section of the calorimeter. Muons are identified as charged particles in the tracker that leave hits in the muon chambers located outside the calorimeter. If isolated high momentum muons are found in the event, $\vec{\not\!\!E}_T$ is corrected by subtracting the average muon ionization energy released in the calorimeter and adding the muon p_T to the vector sum. No specific tau identification algorithm is used in this analysis and in Ref. [11]. Events with τ leptons decaying leptonically are sometimes collected in the data set analyzed in Ref. [11] by identifying their e or μ decay products, while the event selection described here collects hadronic τ decays whenever the decay products are reconstructed as jets. We veto events with reconstructed electrons and muons in order to keep this sample statistically independent from the one analyzed in Ref. [11].

The critical part of this analysis is the requirement of the $\not\!\!E_T$ signature. The $\not\!\!E_T$ in the event can stem not only from neutrinos, but also from various instrumental and detector effects. Events containing large $\not\!\!E_T$ could have originated from noncollision sources, such as cosmic or beam-halo muons passing through the detector or noisy or dead calorimeter cells causing an energy imbalance. These types of events are removed by requiring that the event observables indicate an inelastic collision with large momentum transfer, such as the presence of at least one high quality primary vertex in the collision and at least one central jet with $E_T > 10$ GeV. Additional requirements are also imposed to remove events consistent with beam-halo muons traversing the detector or those caused by noisy calorimeter cells. After these requirements, the leading source of $\not\!\!E_T$ is jet energy mismeasurement due to either jets pointing to noninstrumented regions of the calorimeter, or to calorimeter resolution effects. Both categories of events are characterized by $\vec{\not\!\!E}_T$ often being aligned with the projection of one of the jet three-momenta ($\vec{j}$) in the azimuthal plane. Other characteristic properties of this instrumental background will be described in Sec. VI, together with the strategy devised to suppress it.

V. SIGNAL AND BACKGROUND MODELING

A. Signal modeling

The single top quark production is simulated assuming a top quark mass of 175 GeV/c^2 using the MADEVENT [33] matrix element generator, interfaced to the CTEQ5L [34] parametrization of the parton distribution functions (PDF). The MADEVENT generator models the polarization of the top quark and the distributions of the final-state decay products accordingly. The transition from final-state colored particles to colorless objects is done through the PYTHIA [35] parton showering and hadronization routines.

It has been shown that the inclusion of the next-to-leading-order diagrams results in an increase in the cross section for s-channel production mode, but does not change significantly its kinematics [6]. The s-channel events are thus generated at leading order and the cross section is scaled to the next-to-leading-order rate [6].

For the t channel, the leading-order process for single top quark production is a $2 \to 2$ process with a b quark in the initial state: $b + u \to d + t$ or $b + \bar{d} \to \bar{u} + t$. Single antitop quark production implies the conjugate processes. As several authors have pointed out [6,36], the distribution of observable jets is not adequately represented by the LO contribution to the t-channel production of the single top quark and it is better predicted by next-to-leading-order calculations. In the latter, the b quark stems from a gluon splitting into a $b\bar{b}$ pair. The $\bar{b}$ quark required by the flavor conservation of the strong interaction is created by LO parton shower programs through backward evolution following the DGLAP scheme [37]. The high-p_T tail of the transverse momentum distribution of the $\bar{b}$ quark is not well modeled by this scheme. The mismodeling is estimated by comparing with a NLO calculation [6]. The modeling of the t-channel single top quark process can be improved by producing simulated events with a matrix element generator, followed by the simulation of the production of observable particles by PYTHIA. For this, two samples are used: one for the leading $2 \to 2$ process, and one for the $2 \to 3$ process with a gluon in the initial state $g + q \to q + t + \bar{b}$. In the latter process, the $\bar{b}$ quark is directly produced in the hard scattering described by the matrix element. It also describes the important high-p_T tail of the $\bar{b}$ quark p_T distribution. The construction of a

Monte Carlo simulated sample following the NLO predictions is done by matching the $2 \rightarrow 2$ and $2 \rightarrow 3$ processes as described in [38].

B. Background modeling

There are numerous standard model processes besides single top quark production that can produce the signature characterized by large $\not\!\!E_T$, relatively low jet multiplicity, and no reconstructed charged leptons. The most significant background at the first stage of the analysis is the QCD multijet production. Although these processes generally do not produce neutrinos, mismeasured jet energies do result in imbalance in the measured transverse energy by which the QCD events can pass the basic selection. Furthermore, QCD b quark pair production yields neutrinos whenever one b hadron decays semileptonically, thus giving additional $\not\!\!E_T$. The background sources for this final state are due mainly to QCD production of heavy-quark pairs ($b\bar{b}$ and $c\bar{c}$) and jets falsely tagged as b jets.

Because of the high production rate for QCD at a hadron collider and the large statistics needed in order to describe this process adequately in an analysis looking for a very small signal, the Monte Carlo simulation of an acceptable amount of QCD events is prohibitive. Moreover, the systematic uncertainties associated with the Monte Carlo simulation of QCD jet production are high. For these reasons, we estimate the QCD background solely from data.

Events collected by the $\not\!\!E_T$ + jets trigger are expected to be composed mostly of QCD production of light-flavor jets. We model the heavy-flavor jets QCD rate and distributions by weighting events without any b-tagging requirement by the probability to tag a jet as a b jet. This probability is extracted from events depleted in the single top quark signal, i.e. events with $50 \leq \not\!\!E_T \leq 70$ GeV and $\Delta\phi(\vec{\not\!\!E}_T, \vec{j}_2) < 0.4$, and two or three jets [28]. The tag rate per jet is evaluated as a ratio of b-tagged to fiducial jets, where the fiducial jets are the ones in the kinematic region where the secondary vertex detection efficiency is nonzero. The tag rate is parametrized in terms of variables sensitive to both the efficiency of the identification of true heavy-flavored objects and the rate of false tags. These variables are the jet E_T, the absolute value of the jet η, the scalar sum of the transverse energies of the jets in the event (H_T), and the fraction of jet p_T carried by the charged particles inside the jet which are significantly displaced from the collision point. To compute the last quantity, all charged particles satisfying $0.5 \leq p_T \leq 200$ GeV/c are used, and they are required to have the distance of closest approach to the beam line (d_0) significantly displaced from the beam line, i.e. $|d_0/\sigma_{d_0}| > 2.5$ where σ_{d_0} is the uncertainty on d_0.

The tag rate parametrization is then used to estimate the probability that a fiducial jet in the signal candidate sample is tagged. We construct three independent parametrizations to estimate the background in events with exactly one SECVTX-tagged jet (1S), two SECVTX-tagged jets (2S category), and one SECVTX-tagged and one JETPROB-tagged jet (SJ category). Events which belong to both 2S and SJ categories are assigned to the 2S subsample. Events with three b-tagged jets are discarded. In this way the three selections are orthogonal by construction so that an event can belong to only one category.

By summing the probability of b tagging each fiducial jet in each b-tag subsample and weighting the rate and distributions of data events before any b-tagging requirement (pretag sample), we predict the rate of QCD b-tagged jet multijet production background events and its kinematic distributions. We predict the kinematic properties of events with one SECVTX-tagged jet QCD background from the pretag sample, and the kinematic properties of QCD background events in the 2S and SJ categories from events with one SECVTX-tagged jet. The parametrizations do not completely account for the fact that events with pair production of heavy flavor have enhanced probability to be tagged. For this reason, the normalization of the background events arising from the simple application of the parametrization needs to be scaled. This normalization procedure is described in the next section. The performance of the parametrizations and of the resulting estimate is shown in Fig. 2 where we compare our background model to data in a QCD-dominated region containing events with $\not\!\!E_T > 70$ GeV and $\Delta\phi(\vec{\not\!\!E}_T, \vec{j}_2) < 0.4$. We see that the tag rate parametrization produces a good modeling of the kinematic properties of the QCD events. When building the QCD model in samples containing sizable contributions of the non-QCD process such as W + jets production, we apply the tag rate parametrization to our Monte Carlo simulation of non-QCD processes, and subtract the output from the QCD background estimate. The normalization of the QCD background contribution is set as a scale factor derived in a control region, which multiplies the prediction obtained with the tag rate parametrization, as described in the next section.

The other backgrounds to single top quark production in this signature come from the production of a W or a Z boson in association with jets, top quark pair production through strong interactions, and pair production of heavy vector bosons. All these background processes are simulated using the PYTHIA Monte Carlo simulation program.

We normalized the W and Z boson + heavy flavor jets backgrounds using the inclusive cross sections measured by CDF [39]. The measurements correspond to a factor of 1.4 with respect to the PYTHIA LO predictions. In this way, Z/W boson samples have the correct normalization with respect to their inclusive production. However, the heavy-flavor production simulated by PYTHIA provides a possible source of systematic error. We assign a 40% uncertainty based on the total uncertainty of the Z + heavy flavor jets cross section measurement in CDF [40]. The production of

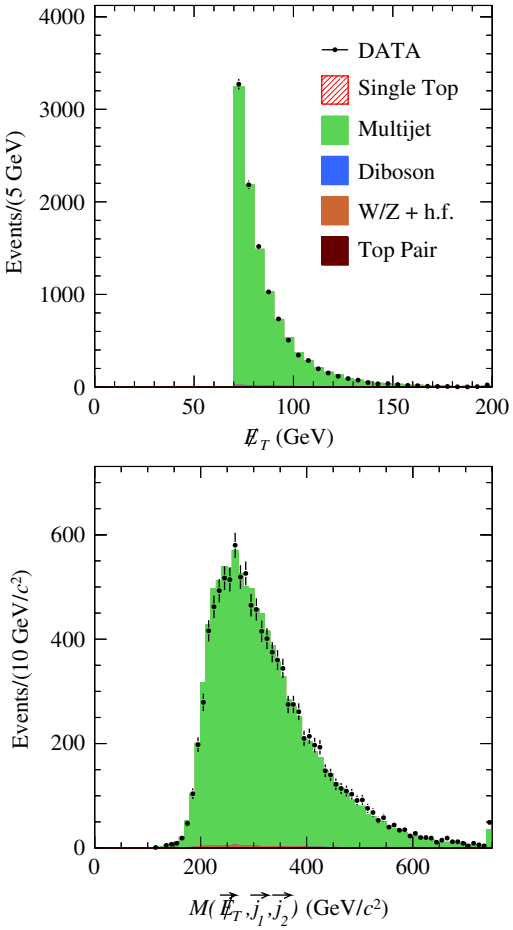

FIG. 2 (color online). Comparison of the background modeling to data in a QCD-dominated control region. The shaded (green) area represents the multijet background model, while the points represent the data. The bin at the right end of the x axis represents the overflow bin. The distributions of the observables under study show good agreement between data and the background model.

W and Z bosons in association with light-flavor jets is included in the multijet modeling.

Top quark pair production yields a non-negligible contribution to the background in the signal region. Because of the large top quark mass and the leptonic decay of the W boson originating from the top quark, these events are energetic, have large $\not\!\!E_T$, and have high jet multiplicity. As for the signal events, in this analysis simulated $t\bar{t}$ events were generated assuming a top quark mass of 175 GeV/c^2. The cross section corresponding to that mass has been computed to be 6.7 ± 0.8 pb [1].

For the simulated diboson samples we use LO cross sections scaled by a factor corresponding to the ratio between the NLO and LO cross section prediction in MCFM [41]. The boson decays are set to be inclusive. An 11.5% uncertainty on the MCFM cross section is assigned to the diboson normalization [42].

VI. EVENT SELECTION

A. Preselection and topology requirements

We define the signal region by selecting events in the kinematic region where the trigger is highly efficient: $\not\!\!E_T > 50$ GeV, $E_T^{j_1} > 35$ GeV and $E_T^{j_2} > 25$ GeV, $\Delta R(\vec{j}_1, \vec{j}_2) > 1$ and by requiring the number of jets to be no more than three, thus accepting events with extra radiation from the incoming or outgoing partons, or hadronically decaying taus reconstructed as jets. In the case of three jet events, the jet with lowest E_T is required to have $E_T^{j_3} \geq 15$ GeV. Events with four or more jets with $E_T > 15$ GeV and $|\eta| < 2.4$ are rejected to reduce backgrounds from QCD and $t\bar{t}$ production. We veto events containing well-identified electrons or muons as identified in Ref. [13] to ensure the independence of the analyzed samples. About 523 000 events pass these preselection requirements, where the s/b ratio for single top quark events after this selection is about 1/2 800 assuming SM cross sections. At this stage of the analysis, the vast majority of the background events are QCD events where mismeasurement of the jet energies gives the very large $\not\!\!E_T$. These events are characterized by having $\vec{\not\!\!E}_T$ aligned in the aximuthal angle ϕ with one of the jets ($\vec{j}_i$) in the event, where the index i runs over the jets in the event. We require $\Delta\phi(\vec{\not\!\!E}_T, \vec{j}_1) > 1.5$ and $\Delta\phi(\vec{\not\!\!E}_T, \vec{j}_{2,3}) > 0.4$ to reject such events. These cuts remove about an order of magnitude of QCD events, but still leave us with a s/b of $\sim 1/340$, where the majority of the background is still composed of QCD multijet production. Finally, we require the presence of at least one jet identified as originating from a b quark. We divide the sample in the three exclusive subsamples 1S, SJ, and 2S defined in Sec. V. This requirement brings the average s/b ratio over the three subsamples to $\sim 1/50$, where the QCD background is still the dominant one. Thus, we need to exploit additional properties of these events in order to further increase the purity of the sample.

B. Neural network-based event selection

We introduce here a neural network approach to the event selection to recognize and separate QCD multijet events with mismeasured jets in which $\not\!\!E_T$ is due to instrumental effects from events with $\not\!\!E_T$ originating from neutrinos. In addition, the neural network is designed to reject events with mistagged light-flavor jets. Using a neural network instead of a "cut-cascade" approach to event selection allows the exploitation of the correlation between the many observables which provide discrimination between signal and backgrounds, and gives a single output thus simplifying the determination of the optimal cut. The neural network model chosen is the multilayer perceptron [43] as implemented in the TMVA package [44], found in ROOT [45].

In this analysis the charged particle spectrometer is used in an innovative way to discriminate between events con-

taining high energy neutrinos and QCD events. We introduce here the imbalance in the momentum flow in the transverse plane, and name it missing transverse momentum, or $\vec{\not\!\!p}_T$, in analogy with the missing transverse energy, $\vec{\not\!\!E}_T$. To compute $\vec{\not\!\!p}_T$, we select charged particles with $0.5 < p_T < 200$ GeV/c and z position at the beam line compatible with the z position of the primary vertex. The missing transverse momentum is then defined as $\vec{\not\!\!p}_T = -\sum_{\text{tracks}} \vec{p}_T$. In collisions producing high energy neutrinos, the magnitude of $\vec{\not\!\!p}_T$ ($\not\!\!p_T$) is proportional to the neutrino energy, while $\vec{\not\!\!p}_T$ provides a good estimate of the neutrino direction. In QCD events with the $\not\!\!E_T$ plus jets topology, where high energy neutrinos are rarely produced and the fluctuation of the charged-to-neutral ratio in jet fragmentation is the primary source of imbalance of the total transverse momentum, the magnitude of $\not\!\!p_T$ is expected to be relatively low, and the vector $\vec{\not\!\!p}_T$ to be often aligned in the direction with the momentum of one of the most energetic jets.

As inputs into our neural network we use the following variables which describe the energy and momentum flow in the detector: the absolute amount of the missing transverse energy $\not\!\!E_T$; the absolute amount of the missing transverse momentum $\not\!\!p_T$; the $\not\!\!E_T$ significance defined as $\not\!\!E_T/\sqrt{\sum E_T}$, where $\sum E_T$ is a scalar sum over the energy deposited in the calorimeter towers; the ratio of $\not\!\!E_T$ to H_T; the ratio of $\not\!\!H_T = |-\sum_{\text{jets}} \vec{p}_T|$ and $\not\!\!E_T$; the invariant mass of $\vec{\not\!\!E}_T$, $\vec{j}_1$ and $\vec{j}_2$, $M(\vec{\not\!\!E}_T, \vec{j}_1, \vec{j}_2)$.

We use the following angular variables: the azimuthal difference between $\vec{\not\!\!p}_T$ and $\vec{\not\!\!E}_T$, $\Delta\phi(\vec{\not\!\!p}_T, \vec{\not\!\!E}_T)$; the maximum of $\Delta\phi$ between any two jets $\vec{j}_i$, $\vec{j}_k$, $\max(\Delta\phi(\vec{j}_i, \vec{j}_k))$; the maximum of the difference in R between any two jets $\vec{j}_i$, $\vec{j}_k$, $\max(\Delta R(\vec{j}_i, \vec{j}_k))$; the minimum of the difference in ϕ between $\vec{\not\!\!E}_T$ and any jet $\vec{j}_i$, $\min(\Delta\phi(\vec{\not\!\!E}_T, \vec{j}_i))$; the minimum of the difference in ϕ between the $\vec{\not\!\!p}_T$ and any jet $\vec{j}_i$, $\min(\Delta\phi(\vec{\not\!\!p}_T, \vec{j}_i))$; the difference in the azimuthal plane between the axis defined by the two most energetic jets in their rest frame, and the vector sum of the two jets in the lab frame, ϕ^*; the event sphericity [46].

We also use variables that discriminate between the fragmentation properties of heavy-flavor quark jets and jets originating from light-flavor quarks or gluons: by taking the charged particles with $p_T > 0.5$ GeV/c and $|d_0/\sigma_{d_0}| > 2.5$ and contained inside the jet cone, we build the variable $\sum p_T^{\text{chgd}}/p_T^j$ for the E_T leading and second leading jets. The 15 variables used as inputs to the neural network are summarized in Table I.

Comparisons of the kinematic distributions for background and signal events for the 15 variables are shown in Figs. 3 and 4, where for simplicity the three subsamples 1S, 2S, and SJ are combined.

The QCD background kinematics do not vary significantly with the heavy-flavor content so only one neural network is used for the three b-tagged subsamples. The single top quark signal used for the training is a mixture of Monte Carlo simulated s-channel events (50%) and t-channel events (50%), which corresponds to the predicted signal composition after preselection. For the background, we use the multijet background model described in Sec. V. All samples are split into two subsamples: one for training the neural network, and one for making predictions of the neural network output and for testing for overtraining. The distributions for training and testing samples are in good agreement. Both samples contain 21 000 signal and 14 000 multijet background events.

TABLE I. Input variables to the neural network devised to suppress the multijet background.

Variable	Description
$\not\!\!E_T$	Absolute amount of the missing transverse energy
$\not\!\!p_T$	Absolute amount of the missing transverse momentum
$\not\!\!E_T/\sqrt{\sum E_T}$	Missing E_T significance
$\not\!\!E_T/H_T$	Ratio of $\not\!\!E_T$ to H_T
$\not\!\!H_T/\not\!\!E_T$	Ratio of $\not\!\!H_T$ to $\not\!\!E_T$
$M(\vec{\not\!\!E}_T, \vec{j}_1, \vec{j}_2)$	Invariant mass of $\not\!\!E_T$, $\vec{j}_i$, and $\vec{j}_2$
$\Delta\phi(\vec{\not\!\!E}_T, \vec{\not\!\!p}_T)$	Azimuthal difference between $\not\!\!E_T$ and $\not\!\!p_T$
$\max(\Delta\phi(\vec{j}_i, \vec{j}_k))$	Maximum of $\Delta\phi$ between any two jets $\vec{j}_i$, $\vec{j}_k$
$\max(\Delta R(\vec{j}_i, \vec{j}_k))$	Maximum of ΔR between any two jets $\vec{j}_i$, $\vec{j}_k$
$\min(\Delta\phi(\vec{\not\!\!E}_T, \vec{j}_i))$	Minimum of $\Delta\phi$ between $\vec{\not\!\!E}_T$ and any jet $\vec{j}_i$
$\min(\Delta\phi(\vec{\not\!\!p}_T, \vec{j}_i))$	Minimum of $\Delta\phi$ between $\vec{\not\!\!p}_T$ and any jet $\vec{j}_i$
ϕ^*	$\Delta\phi$ between the $(\vec{j}^1, \vec{j}^2)$ axis in their rest frame, and their vector sum in the lab frame
Sphericity	$S = \frac{3}{2}(\lambda_2 + \lambda_3)$ [46]
$\sum p_T^{\text{chgd}}/p_T^{j_1}$	Fraction of $p_T^{j_1}$ carried by charged particles displaced from the primary vertex
$\sum p_T^{\text{chgd}}/p_T^{j_2}$	Fraction of $p_T^{j_2}$ carried by charged particles displaced from the primary vertex

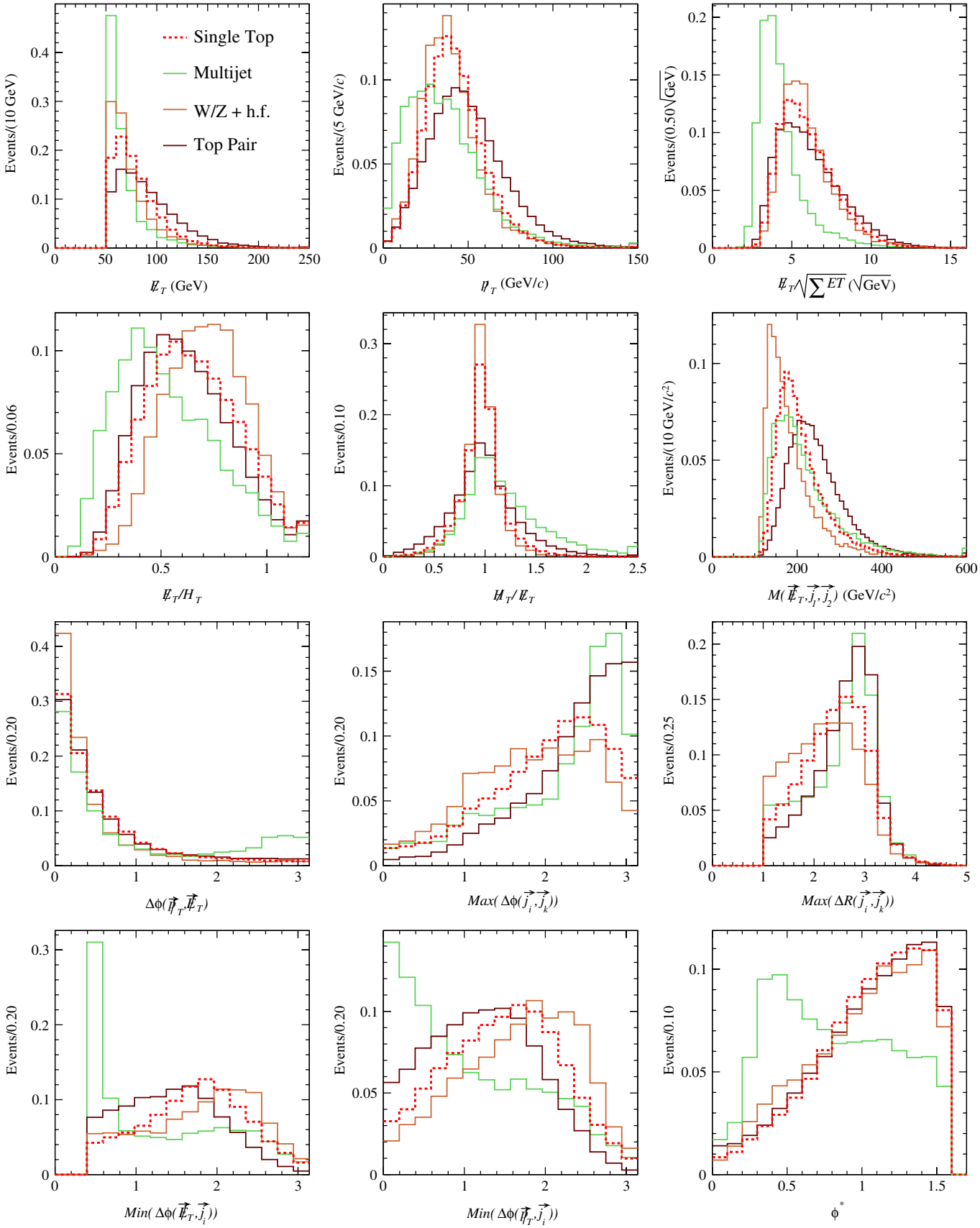

FIG. 3 (color online). Kinematic distributions for signal and background events passing the event preselection. The three subsamples are summed together in their respective proportions. All histograms are normalized to unit area.

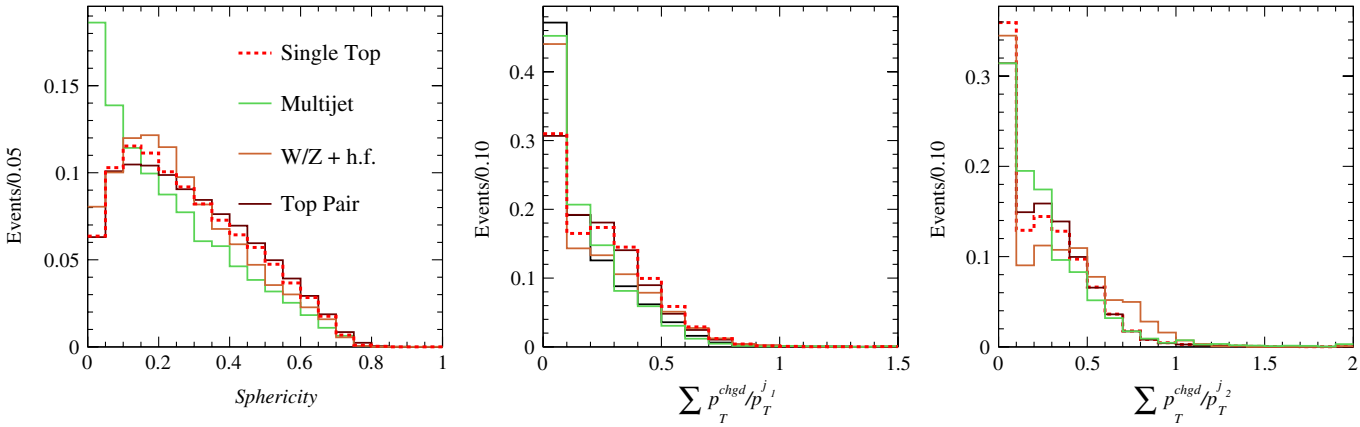

FIG. 4 (color online). Kinematic distributions for signal and background events passing the event preselection. The three subsamples are summed together in their respective proportions. All histograms are normalized to unit area.

Among the configurations investigated, the one which performs best uses all 15 variables defined above as inputs, two hidden layers with 30 and 15 nodes, respectively, and one output node. Figure 5 shows the distribution of the value of the output node, $\mathrm{NN_{QCD}}$.

The signal region is defined as the sample of events surviving the cut on $\mathrm{NN_{QCD}}$ devised to maximize the background rejection while retaining high signal efficiency. By requiring $\mathrm{NN_{QCD}} > -0.1$, we reduce the multijet contribution by 77%, while keeping 91% of the signal.

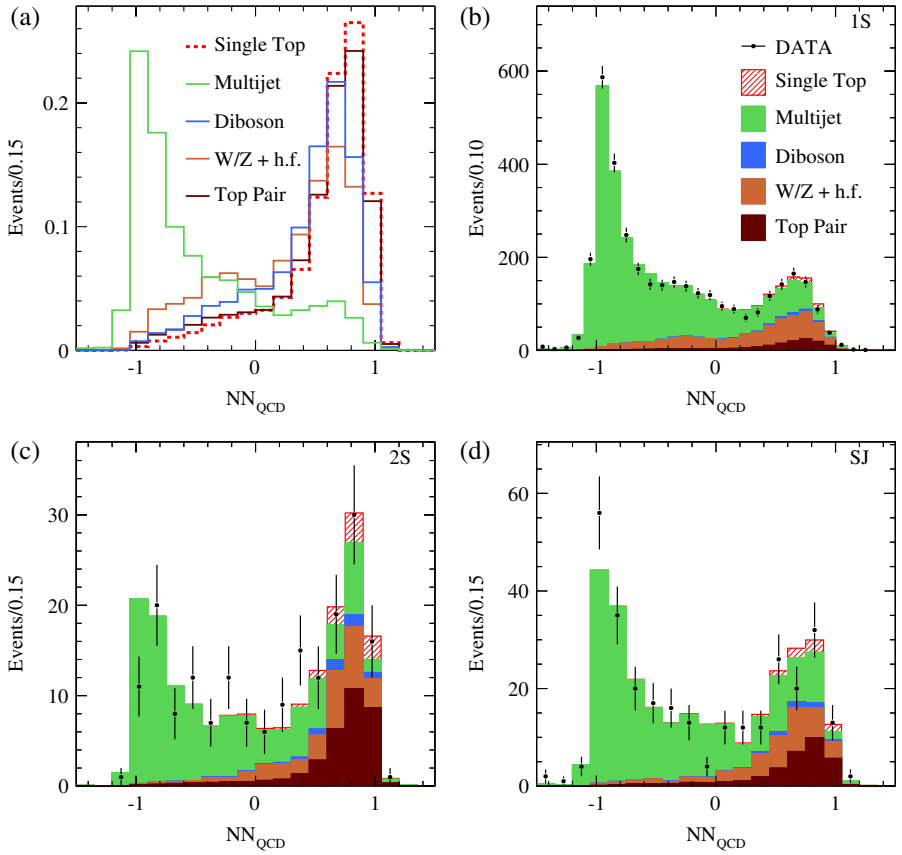

FIG. 5 (color online). Distributions of the $\mathrm{NN_{QCD}}$ output for events passing the event preselection. (a) shows the distribution for the signal and the backgrounds normalized to unity. The remaining three plots show the same distribution for the three subsamples, 1S (b), 2S (c), and SJ (d), where the background and signal predictions are stacked according to predictions, and compared to data events. As can be seen from the plots, the kinematics of the QCD background events are very different from the signal and the other backgrounds. These events are removed using the cut $\mathrm{NN_{QCD}} < -0.1$. The remaining events are used to scan for the presence of the single top quark signal.

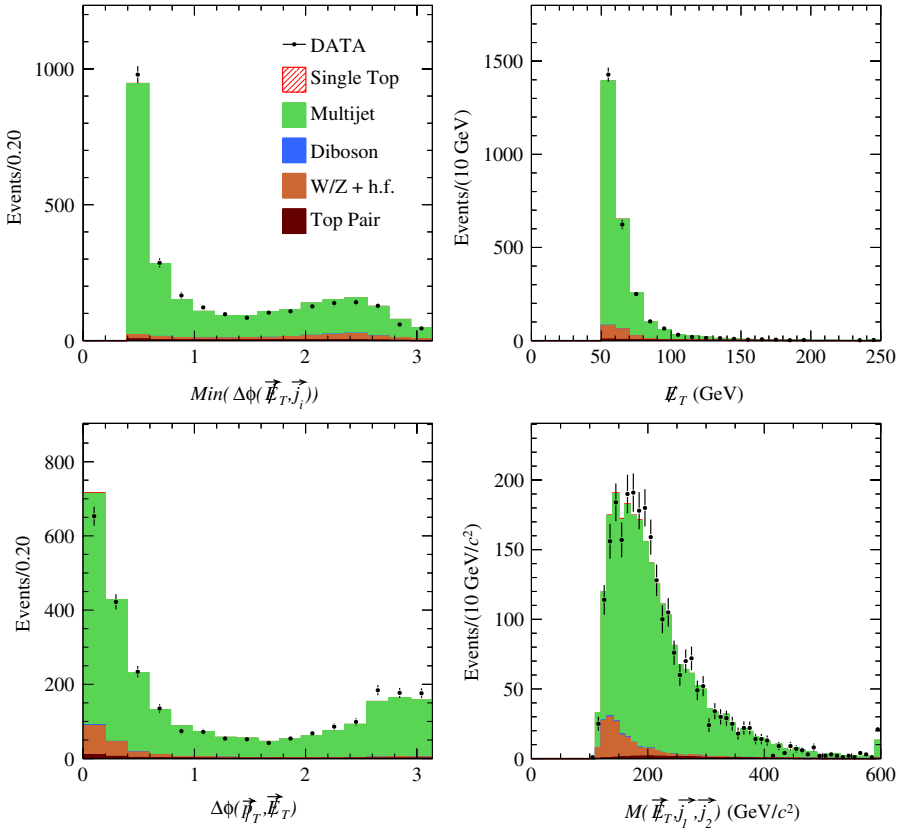

FIG. 6 (color online). Comparison of the QCD background modeling to data in the $\mathrm{NN_{QCD}} < -0.1$ control region. The three subsamples are summed together in their respective proportions. Good agreement is visible between data and the background model.

The overall backgrounds are reduced by 65% thus bringing the s/b ratio from $1/50$ to $1/20$. The signal significance $s/\sqrt{s+b}$ is increased by 50%, from 1.2 to 1.7. We look at the background-dominated region with $\mathrm{NN_{QCD}} < -0.1$ to verify that the background model properly describes the data. Figure 6 shows distributions of data events superimposed to the sum of the expected backgrounds; the background model properly describes the data within uncertainties. Moreover, data events in the same region are used to compute the normalization for multijet production, by comparing the prediction given by weighting the events for the tag rate parametrization, and the observed number of data events. We find that the predictions must be multiplied by scale factors that depend on the combination of b-tagging algorithms used. The values extracted are 1.08 ± 0.05 for events in the 1S subsample, 0.79 ± 0.10 for 2S events, and 0.76 ± 0.07 for SJ events. Table II shows the contribution of signal and background events in the signal sample, divided into three subsamples under study. After requiring $\mathrm{NN_{QCD}} > -0.1$, the dominant backgrounds are from multijet production, W/Z + heavy flavor jets events, and $t\bar{t}$ events. The multijet contribution after the $\mathrm{NN_{QCD}} > -0.1$ cut now primarily consists of events with true missing energy coming from a W or Z boson, accompanied by light-flavor jets misidentified as b jets.

We use our simulated single top quark data sample to investigate which decay modes of the W bosons from top quark decays survive the event selection including the lepton veto. We find that the largest category of single

TABLE II. Number of predicted and observed events in the signal region defined by requiring $\mathrm{NN_{QCD}} > -0.1$ in the subsample with exactly one SECVTX-tagged jet (1S), two SECVTX-tagged jets (2S), and one SECVTX- and one JETPROB-tagged jet (SJ). The notation "h.f." stands for heavy-flavor jets. The uncertainty in the predicted number of events is due to the theoretical cross section uncertainty and to the uncertainty on signal and background modeling.

Process	$1b$ tag (1S)	$2b$ tags (2S)	$2b$ tags (SJ)
s channel	15.7 ± 2.0	7.6 ± 0.9	6.3 ± 0.8
t channel	31.2 ± 4.9	1.7 ± 0.2	1.6 ± 0.2
$t\bar{t}$	125 ± 23	30.3 ± 5.8	29.2 ± 5.7
$WW/WZ/ZZ$	33.0 ± 6.5	4.9 ± 0.6	4.2 ± 0.6
W + h.f.	269 ± 113	12.7 ± 7.5	22.7 ± 13.7
Z + h.f.	105 ± 53	11.8 ± 5.8	11.8 ± 6.0
Multijet	592 ± 27	28.9 ± 3.8	58.5 ± 5.8
Total	1172 ± 169	98 ± 15	134 ± 21
Observed	1167	113	131

top quark decays is $W \to \tau\nu$ ($\sim 50\%$ of decays), followed by $W \to \mu\nu$ ($\sim 30\%$), and $W \to e\nu$ ($\sim 20\%$). The presence of hadronic W decays is suppressed by the requirement of large $\not\!\!E_T$, and by the $\mathrm{NN_{QCD}} > -0.1$ cut, so that the fraction of all-hadronic single top decays is found to be negligible.

VII. DISCRIMINATING THE SIGNAL FROM REMAINING BACKGROUNDS

In the previous section we described an event selection which enhances the signal purity of the sample by suppressing the presence of backgrounds that do not produce real neutrinos. At this stage of the analysis, the s/b is about $1/20$, where the main background processes all produce neutrinos. Unfortunately, all of the surviving backgrounds have topology and kinematics which are very similar to single top quark events. In addition, the systematic uncertainty on the background prediction is approximately 2 to 4 times the size of the signal we seek, depending on the subsample.

Further discrimination of the signal from the background is required. In order to increase the statistical power of the analysis, and to minimize the effect of the background systematic uncertainties, we study the signal sample to take advantage of the small residual differences between the signal and backgrounds. Another neural network will be used for this purpose, where events which appear to be more signal-like are used to test for the presence of single top quark production and to measure the cross section, and events which appear to be more background-like are used to constrain the uncertain background rates.

We use the following variables to discriminate between signal and background processes: the invariant mass of $\vec{j}_2$ and $\not\!\!\vec{E}_T$, $M(\vec{j}_2, \not\!\!\vec{E}_T)$; H_T; $\min(\Delta\phi(\not\!\!\vec{E}_T, \vec{j}_1))$; $\sum p_T^{\mathrm{chgd}}/p_T^{j_1}$; $\sum p_T^{\mathrm{chgd}}/p_T^{j_2}$; $\not\!\!E_T$; $\not\!\!p_T$; ϕ^*; $\not\!\!E_T/H_T$; $M(\not\!\!\vec{E}_T, \vec{j}_1, \vec{j}_2)$; the invariant mass of all jets, M(all jets). All the above observables are used as inputs to a multilayer-perceptron neural network trained to distinguish the signal from backgrounds in the sample with $\mathrm{NN_{QCD}} > -0.1$. We use the simulated single top quark s- and t-channel samples in their expected proportions to build the signal sample (approximately 50%-50%). For training purposes, we select the background processes which account for more than 5% of the total background: multijet, $W \to \tau\nu$ plus heavy-flavor jets, $Z \to \nu\nu$ plus heavy-flavor jets, and $t\bar{t}$ production. Both training and test samples contain 39 000 signal and 42 000 background events. The network architecture consists of an input layer with 11 nodes corresponding to the input variables shown in Table III, plus one bias node; one hidden layer with 22 nodes and one hidden layer with 11 nodes, and an output layer with one output node, which we label $\mathrm{NN_{sig}}$. We compare the $\mathrm{NN_{sig}}$ output distribution between the training and testing samples and find good agreement. The distributions of the input variables for events in the signal region, for all b-tagged subsamples, are shown in Fig. 7, where the shapes of the distributions for each group of physics processes are compared. Figure 8 shows that the predictions agree well with the observed data. The output of $\mathrm{NN_{sig}}$ is shown in Fig. 9, where the contributions from the signal and main backgrounds are normalized to unit area. The single top quark signal events populate mostly the region of $\mathrm{NN_{sig}}$ around 0.3, while background events populate mostly the region with $\mathrm{NN_{sig}}$ around -0.3. Finally, the same distribution is shown in Fig. 10, where the signal and background contributions have been normalized according to their estimates in the three subsamples, and the data are superimposed.

TABLE III. Input variables to the neural network aimed at discriminating single top quark production from the backgrounds remaining after the $\mathrm{NN_{QCD}} > -0.1$ requirement.

Variable	Description
$M(\not\!\!\vec{E}_T, \vec{j}_2)$	Invariant mass of $\not\!\!E_T$ and $\vec{j}_2$
H_T	Scalar sum of the jet energies
$\min(\Delta\phi(\not\!\!\vec{E}_T, \vec{j}_i))$	Minimum of $\Delta\phi$ between $\not\!\!\vec{E}_T$ and any jet $\vec{j}_i$
$\sum p_T^{\mathrm{chgd}}/p_T^{j_1}$	Fraction of $p_T^{j_1}$ carried by charged particles displaced from the primary vertex
$\sum p_T^{\mathrm{chgd}}/p_T^{j_2}$	Fraction of $p_T^{j_2}$ carried by charged particles displaced from the primary vertex
$\not\!\!E_T$	Missing transverse energy
$\not\!\!p_T$	Missing transverse momentum
ϕ^*	$\Delta\phi$ between the $(\vec{j}^1, \vec{j}^2)$ axis in their rest frame, and their vector sum in the lab frame
$\not\!\!E_T/H_T$	Ratio between $\not\!\!E_T$ and H_T
$M(\not\!\!\vec{E}_T, \vec{j}_1, \vec{j}_2)$	Invariant mass of $\not\!\!E_T$, $\vec{j}_i$, and $\vec{j}_2$
M (all jets)	Invariant mass of all jets in the event

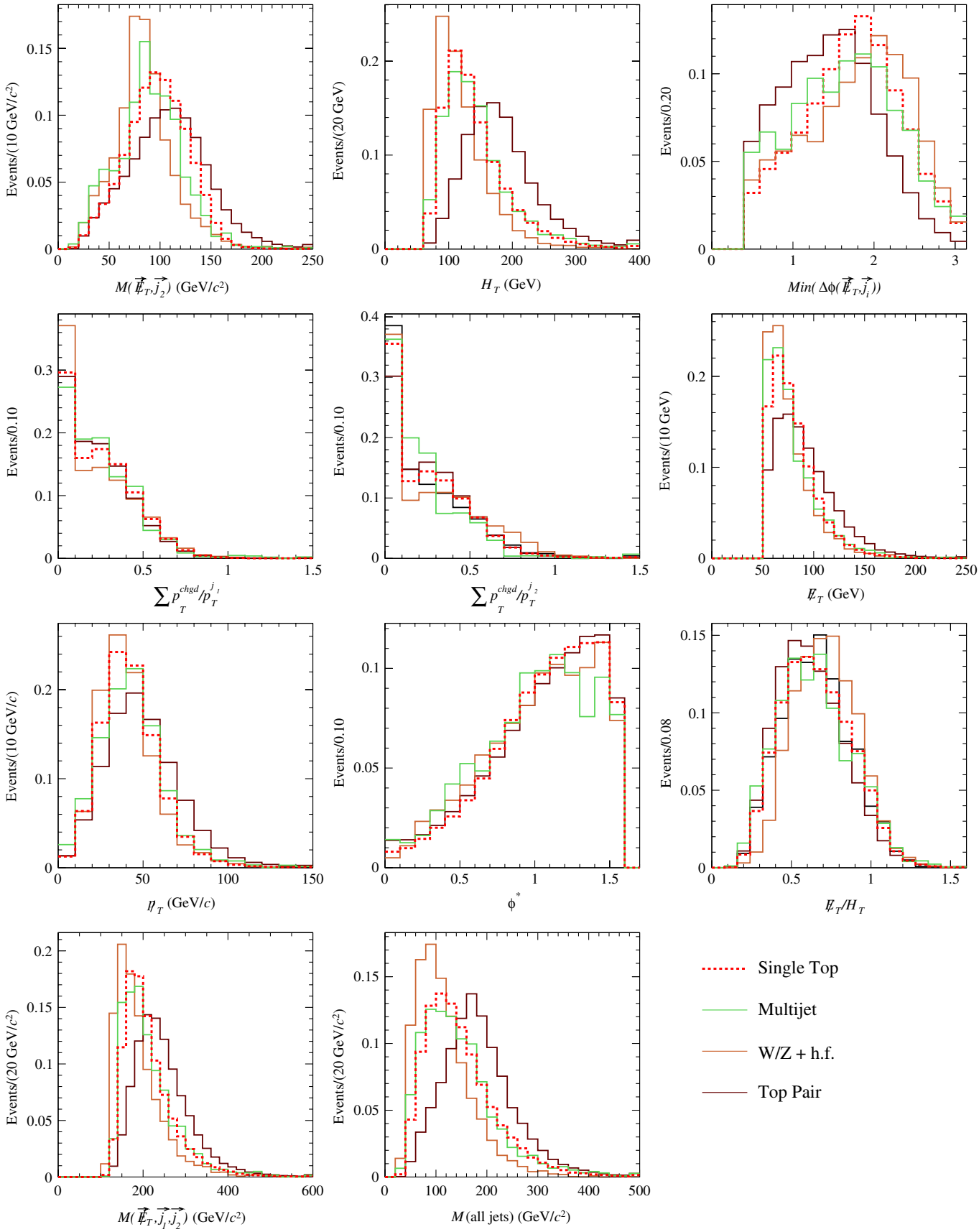

FIG. 7 (color online). Kinematic distributions for the signal and background events in the signal region ($NN_{QCD} > -0.1$). The three subsamples are summed together in their respective proportions. All histograms are normalized to unit area.

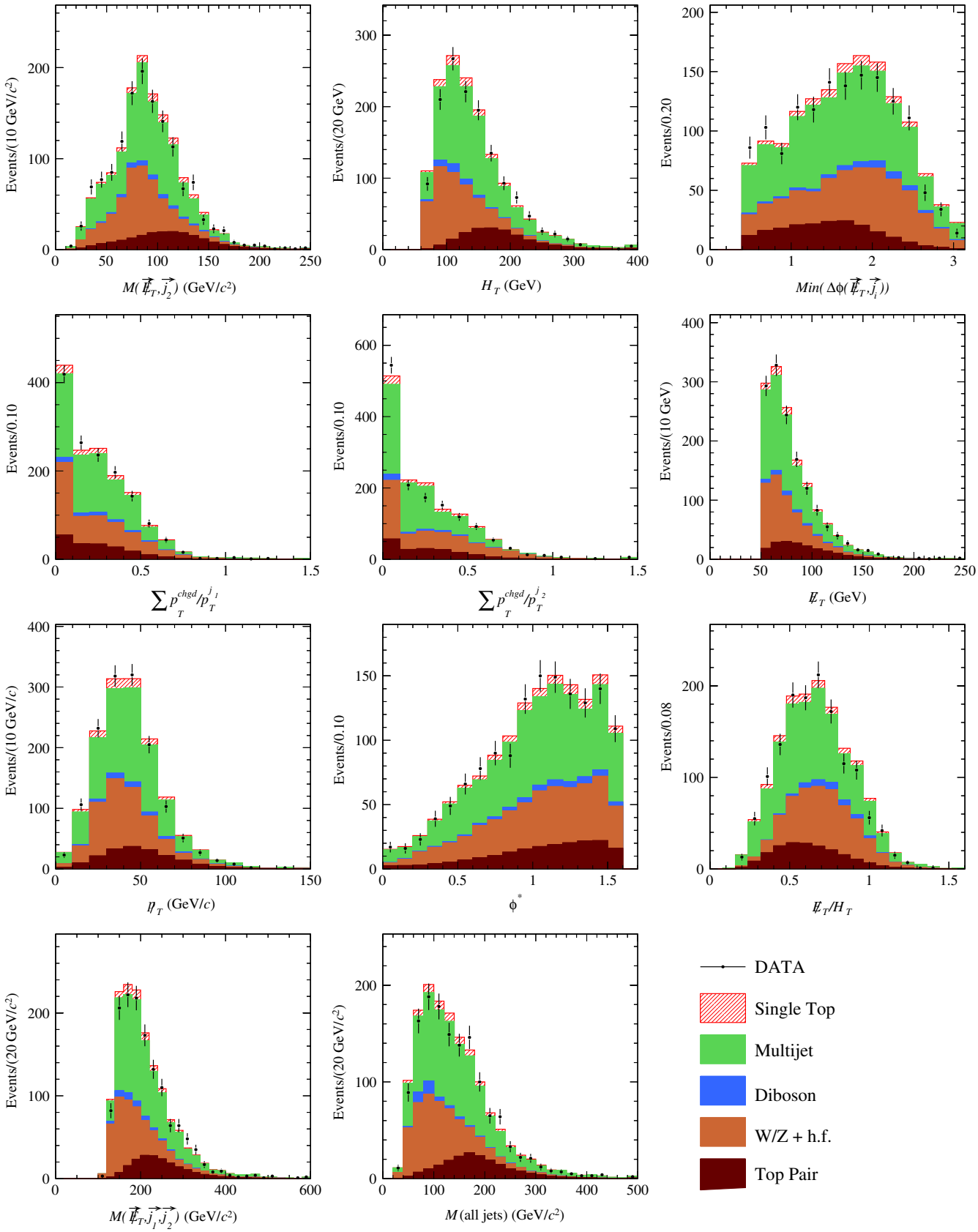

FIG. 8 (color online). Kinematic distributions for the signal and background events in the signal region ($NN_{QCD} > -0.1$). The three subsamples are summed together in their respective proportions. All physics processes contributions are normalized to the expected amount of events, as described in Sec. V.

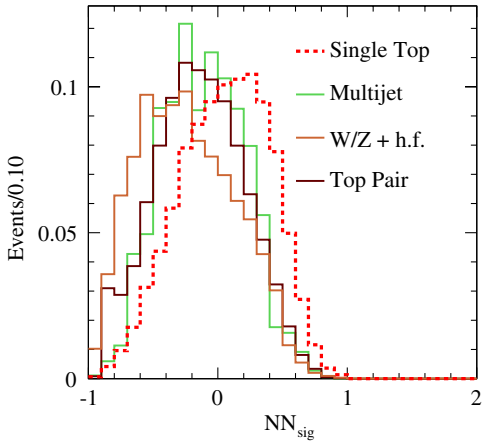

FIG. 9 (color online). Distribution of NN_{sig} for the signal and main background processes in the signal region. The three subsamples are summed together in their respective proportions. All histograms are normalized to unity. A small but important residual discrimination of the signal from the backgrounds is obtained.

VIII. SYSTEMATIC UNCERTAINTIES

Systematic uncertainties are grouped by their sources, where a given source of uncertainty may affect several background and signal distributions. The various systematic uncertainties originating from the same source are considered 100% correlated. There are two categories of systematic uncertainties. Rate uncertainties are related to the predicted production rates, efficiency and acceptance of the various signal and background processes. Shape uncertainties express differences in the distributions due to a given systematic source. Some sources of systematic uncertainty affect both rates and shapes. All rate uncertainties are assigned a truncated Gaussian prior, preventing negative predictions. For shape uncertainties, if the prediction for a given bin is negative, it is set to zero.

A. Theoretical cross sections

For all physics processes modeled by Monte Carlo simulation, we normalize to the most up-to-date theoretical computation of the cross section, and corresponding uncertainties. We use 12% uncertainty for top quark pair production [1], 40% uncertainty for the W and Z background processes [40], and 11% for the diboson prediction [42].

B. Integrated luminosity

This systematic source accounts for the uncertainty in the $p\bar{p}$ inelastic cross section and for the uncertainty in the acceptance of the luminosity monitor of CDF to inelastic $p\bar{p}$ collision events [47] and it is estimated as 6%. This

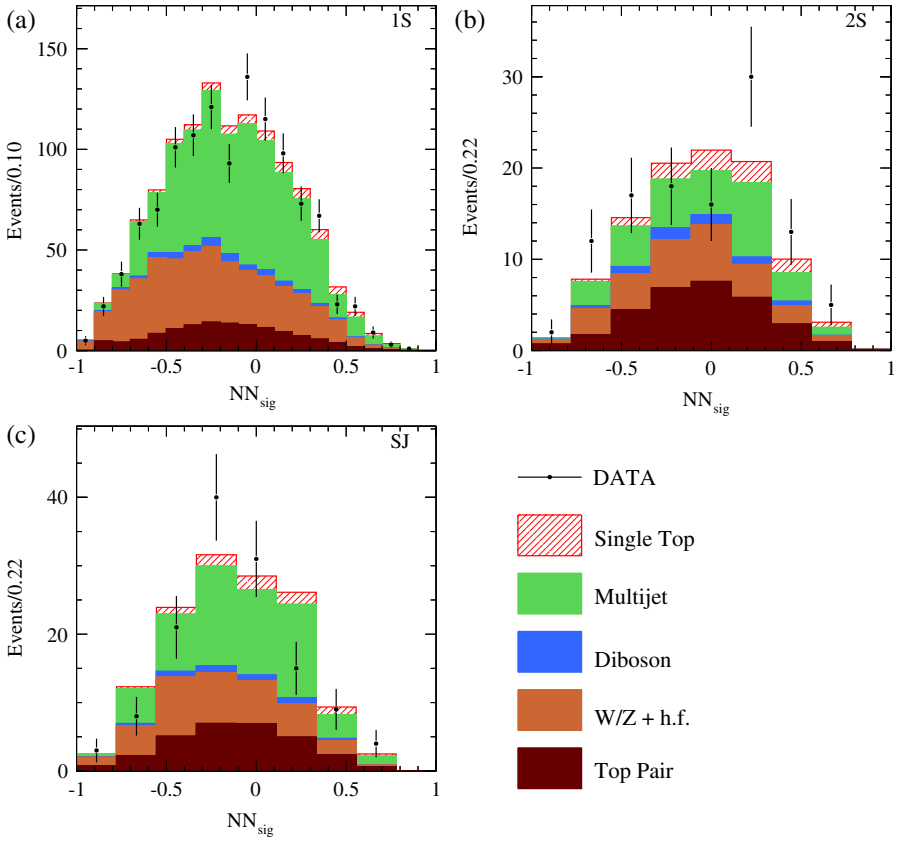

FIG. 10 (color online). NN_{sig} discriminant output distributions in signal region, for the 1S subsample (a), 2S (b), and SJ (c).

uncertainty is applied to the rate predictions based on Monte Carlo simulation, i.e. all processes apart from multijet production.

C. Trigger efficiency

Since we are using data below the fully efficient region of the trigger, we apply a parametrization of the trigger efficiency to the Monte Carlo simulated backgrounds. We assign a systematic uncertainty to both Monte Carlo simulated backgrounds and signal acceptances by varying the trigger efficiency parameters [28].

D. *b*-tagging efficiency

The *b*-tagging efficiency affects the predicted rates of signal and background estimates for which we use Monte Carlo simulations. Known differences between the data and the simulation are corrected by scaling the simulation, and uncertainties on these scale factors are collected together in one source of uncertainty (they affect the predictions in the same way). We assign an uncertainty of 4.3% for the 1S prediction, 8.6% for the 2S, and 12% for SJ.

E. Lepton veto

The uncertainty in the efficiency of the cuts used to veto leptons was determined to be 2%.

F. Initial and final-state radiation (ISR/FSR)

To evaluate the ISR, PYTHIA uses a model of ''backwards evolution'' [35,48]. The model used by PYTHIA for gluon radiation from partons emitted from the hard-scattering interaction has been tuned with LEP data. Monte Carlo simulated samples are generated for single top quark signals and $t\bar{t}$ with Λ_{QCD} doubled (more ISR) or divided in half (less ISR) and with the initial transverse momentum scale and the hard scattering of the shower both multiplied (more ISR) or divided (less ISR) by 4. The parameters for the final-state showering are also adjusted in PYTHIA, except for the hard-scattering scale. The uncertainties are then computed by comparing the efficiencies and kinematics of the varied ISR/FSR events to the nominal ones. The effects of variations in ISR and FSR are treated as 100% correlated with each other.

G. Jet energy scale (JES)

Each step in the correction of the calorimeter response to particle jets involves an uncertainty, which is propagated to the final JES [29]. The effects of JES uncertainties are estimated by varying the jet energy scale in all Monte Carlo simulated samples twice: one upwards, one downwards. They are evaluated for each background and signal contribution, and both rate and shape uncertainties are taken into account.

H. Parton distribution functions

Lack of precise knowledge of the PDFs is a source of theoretical uncertainty for the amount of signal produced. The uncertainty is estimated using different sets of PDF eigenvectors. The default PDF set used in this analysis is the CTEQ5L set [34]. The uncertainty is determined comparing:

(i) two different LO PDF parametrization sets, CTEQ5L [34] and MRST72 [49];
(ii) MRST72 and MRST75 with different Λ_{QCD};
(iii) the variation within their uncertainties of each of the 20 signed eigenvectors of the NLO PDF set CTEQ6M [50] with the default PDF set.

The total PDF uncertainty is obtained adding the larger of the 20 eigenvectors' uncertainty (all added in quadrature) or the MRST72 and CTEQ5L PDF sets uncertainty in quadrature with the Λ_{QCD} uncertainty. A 2% uncertainty was found to be sufficient for all the backgrounds. The PDF uncertainty on the signal acceptance ranges from 1% to 2% depending to the subsample. Shape variations induced by PDF systematic changes are considered only for the single top quark process.

I. Multijet model

The data-driven model for multijet production predicts the shapes of the distributions. The rates are obtained from the $\mathrm{NN}_{\mathrm{QCD}} < -0.1$ control region. In this region, we assign a scale factor associated with the difference between the data rates and the Monte Carlo simulation prediction, which we then multiply to the multijet predicted rate. We then obtain the uncertainty on this scaling using propagation of errors. Depending on the subsample under study, we assign an uncertainty between 4.5% and 13%. The variations in the tag rate probability parametrization used to estimate the multijet background also modify the shapes of the distributions. The shape uncertainty is obtained by varying the tag rate probability by the uncertainty in its estimation. We also take into account the normalization uncertainty on the processes which are part of the background in the region from which we get the QCD normalization. Those uncertainties are anticorrelated with respect to the normalization on these processes, and are weighted appropriately. In the $\mathrm{NN}_{\mathrm{QCD}} < -0.1$ control sample used to derive the normalization, the biggest contamination sources come from W + heavy flavor jets (5% of the 1S and $<1.5\%$ of the 2S and SJ samples), $t\bar{t}$ (2.7% of the 2S sample and $<1.5\%$ of the two other samples), and Z + heavy flavor jets ($< 1.8\%$ of the three *b*-tagged subsamples). Diboson contamination is negligible ($< 0.5\%$). To avoid double counting nonmultijet events in our estimation of the multijet background, we apply the tag rate parametrization to our Monte Carlo simulation predictions and subtract the output from the data. The single top quark signal as predicted by Monte Carlo simulation is also

subtracted from the data. We associate a shape systematic uncertainty to this removal by varying the amount of the single top quark we subtract by 50%, more than 3 times the theoretical uncertainty on the single top quark cross section.

J. Background scaling

A small fraction of the data events analyzed in this paper pass the event selection requiring identified charged leptons in the final state [13]. The fraction has been computed using single top quark Monte Carlo simulation to be 2%. To maintain a 100% orthogonality with Ref. [13], these events are discarded from this analysis. We scale down the predicted amount of background events by 2%, and assign an additional uncertainty of 2% to the background yields.

K. Top quark mass dependence

The most precise measurement of the top quark mass corresponds to $M_{\text{top}} = 173.1 \pm 1.3$ GeV$/c^2$ [51]. We consider for this analysis a nominal top quark mass of $M_{\text{top}} = 175$ GeV$/c^2$ for the acceptance computation and kinematic estimation, and use the two extreme values of 170 and 180 GeV$/c^2$ to compute the systematic shifts. This uncertainty is considered for all processes producing top quarks when extracting the value of V_{tb} and computing the significance of the measurement.

The summary of the systematic sources, their effect on the rates of different processes, and how they affect the kinematics can be found in Table IV.

IX. CROSS SECTION AND SIGNIFICANCE EXTRACTION

We scan the NN_{sig} distribution using a binned likelihood technique to measure its cross section, as well as to determine the significance of the excess itself. The likelihood function L is given by the product of the likelihood for each of the different subsamples L_c, $L = \prod_{c=1}^{N_c} L_c$ where $N_c = 3$ are the three subsamples subdivided according to the number of b-tagged jets and the tagging algorithm used (1S, 2S, SJ). The likelihood L_c for each subsample to observe the data in the final NN distribution is defined as

$$L_c = \prod_{i=1}^{n_{\text{bins}}} P(n_i|\mu_i) = \prod_{i=1}^{n_{\text{bins}}} \frac{\mu_i^{n_i} e^{-\mu_i}}{n_i!}, \tag{1}$$

where n_i is the data count in that particular bin and n_{bins} is the number of bins in the distribution which is scanned to look for an excess of signal-like events. The prediction in each bin is a sum over signal and background contributions:

$$\mu_i = \sum_{k=1}^{n_{\text{bkg}}} b_{ik} + s_i, \tag{2}$$

where b_{ik} is the background prediction in bin i for background source k given the number of background sources n_{bkg} and s_i is the signal prediction in bin i for the s- and t-channel single top quark production summed according to the standard model proportions. Uncertain nuisance parameters $\boldsymbol{\theta}$ affect the signal and background predictions and kinematics. The induced effect on the event rates and shapes of the kinematic distributions can be correlated with

TABLE IV. Summary of systematic uncertainties and their treatment in the analysis. A range of values is listed for a systematic source to indicate that the effect is different in the three subsamples defined by the different heavy-flavor jet content. The "X" sign in the "Shape" column means that the influence of the change in the systematic source on the kinematic distributions of the physics processes has been considered, while the "$\cdots$" sign means that it is not applicable, or not considered. The "Comment" column describes whenever a systematic is considered only for some physics processes, or treated differently for some physics processes, or considered only in certain computations.

Systematic source	Rate	Shape	Comment
Top quark pair production cross section	$\pm 12\%$	$\cdots$	
W/Z + heavy flavor jets cross section	$\pm 40\%$	$\cdots$	
Diboson cross section	$\pm 11\%$	$\cdots$	
Luminosity	6%	$\cdots$	Not for multijet
Trigger efficiency	$<2.6\%$	X	
b-tagging efficiency	4.3% to 12%	$\cdots$	
Lepton veto	2%	$\cdots$	
ISR/FSR	$-4.5\% \cdots + 16\%$	X	Only for top quark processes
JES	$-14\% \cdots + 23\%$	X	
PDF	$\pm 1\% \cdots \pm 2\%$	X	Shape for signal only
Multijet model	$4.5\% \cdots 13\%$	X	
Background scaling	2%	$\cdots$	
Single top quark cross section	$\pm 12\%$	$\cdots$	Only for p value and V_{tb} computation
Top quark mass dependence	$-16\% \cdots + 7.5\%$	X	

each other. The likelihood L is then a function of the observed data $\boldsymbol{D}$, the signal cross section σ_{s+t} and of the nuisance parameters $\boldsymbol{\theta}$ which affect the signal and background predictions, $L(\boldsymbol{D}|\sigma_{s+t}, \boldsymbol{\theta})$. We use Bayes' theorem to convert the likelihood into a posterior density function in σ_{s+t}. We use the posterior density function to quote the measured value of the production rate [52]. The posterior density function is

$$p(\sigma_{s+t}|\boldsymbol{D}) = \frac{1}{N}\int L(\boldsymbol{D}|\sigma_{s+t}, \boldsymbol{\theta})\pi(\boldsymbol{\theta}, \sigma_{s+t})d\boldsymbol{\theta}, \quad (3)$$

where N is an overall normalization obtained from the requirement $\int p(\sigma_{s+t}|\boldsymbol{D})d\sigma = 1$. The function $\pi(\boldsymbol{\theta}, \sigma_{s+t})$ is the prior probability density, which encodes our knowledge of the parameters $\boldsymbol{\theta}$ and σ_{s+t}. Since our knowledge of the cross section is independent of our prior knowledge of the nuisance parameters, we can write the prior density as $\pi(\boldsymbol{\theta}, \sigma_{s+t}) = \pi(\boldsymbol{\theta}) \cdot \pi(\sigma_{s+t})$. The ignorance about the true single top quark production cross section is encoded through the prior probability density function, which is set equal to the Heaviside function in σ_{s+t}, $\pi(\sigma_{s+t}) = 1$ if $\sigma_{s+t} \geq 0$ and $\pi(\sigma_{s+t}) = 0$ otherwise. The prior probability density functions on the nuisance parameters are set to be Gaussian distributions, characterized by the estimated central value of the systematic source and the associated uncertainty. The posterior density function can thus be written as

$$p(\sigma_{s+t}, \boldsymbol{D}) = \frac{1}{N}\int L(\boldsymbol{D}|\sigma_{s+t}, \boldsymbol{\theta})\pi(\boldsymbol{\theta})\pi(\sigma_{s+t})d\boldsymbol{\theta}. \quad (4)$$

The marginalization of the posterior density function is done using Monte Carlo integration, by generating a large number of points in the nuisance parameters space, according to their priors probability density functions.

In doing the generation, we take into account the correlations between nuisance parameters. Shape and rate uncertainties due to a given nuisance parameter are treated as 100% correlated. We define the measured cross section $\sigma_{s+t}^{\text{meas}}$ as the value corresponding to the mode of the $p(\sigma_{s+t}|\boldsymbol{D})$ distribution, and its uncertainty as the smallest interval enclosing 68% of the integral. In order to measure the single top quark production cross section and its uncertainty, we do not include the m_t uncertainty in the $t\bar{t}$ background or in the signal, but rather quote the measurement at the assumed top quark pole mass of $m_t = 175\ \text{GeV}/c^2$. We assume the standard model ratio between s- and t-channel production.

The measured cross section depends on the true cross section but also the random outcome of the data. The sensitivity of the analysis is evaluated using the expected distribution of outcomes, assuming a signal is present. The event selection cut values and the final discriminant used to scan for the signal have been chosen to maximize the expected sensitivity to the signal. We check our cross section fit method using pseudoexperiments generated varying the input signal cross section and systematic uncertainties, which are then fit to measure the signal cross section to check for possible biases. The procedure used cannot produce a negative cross section measurement, since the priors are zero for negative values. For an input cross section of zero, half of the measured cross sections then are exactly zero, and the other half form a distribution of positive fit cross sections. We therefore use the median fit cross section for our linearity check to avoid the bias which would be introduced by using the average instead. Distributions of 68% and 95% of extracted cross sections centered on the medians are then shown as a function of the input cross section in Fig. 11. It can be deduced from the same plot that the fit technique used here does not introduce a bias.

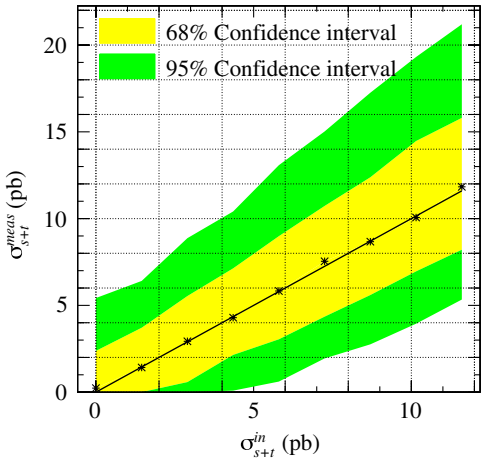

FIG. 11 (color online). Distributions of 68% and 95% of extracted cross sections centered on the medians are shown as a function of a set of input cross section. The line represents $\sigma_{s+t}^{\text{meas}} = \sigma_{s+t}^{\text{in}}$. The plot shows that the fit technique does not introduce bias.

A. Significance calculation

In addition to measuring its cross section, it is also important to estimate the significance of the measurement itself. To do so, we use the p value, which is the probability of observing an outcome of our experiment at least as signal-like as the one observed or more, assuming that a signal is absent. By convention, an observed p value of less than 1.35×10^{-3} constitutes evidence for a signal, and an observed p value less than 2.87×10^{-7} constitutes a discovery. These are the one-sided integrals of the tails of a unit Gaussian distribution beyond $+3\sigma$ and $+5\sigma$, respectively. The experimental outcome is ranked on a one-dimensional scale using the likelihood ratio test statistic [53]:

$$-2\ln Q = -2\ln\frac{L(\boldsymbol{D}|\sigma_{s+t} = \sigma'_{s+t})}{L(\boldsymbol{D}|\sigma_{s+t} = 0)}. \quad (5)$$

In the computation of the $-2\ln Q$ and thus the p value, we

include all sources of systematic uncertainties, including the theoretical uncertainty on the single top quark production cross section and on the top quark mass itself. We perform two sets of a large number of pseudoexperiments and compute corresponding $-2\ln Q$ distributions. In the first one, pseudodata are generated in the hypothesis that single top quark production is present in the SM-predicted amount (S + B). In the second, pseudodata are generated according to the background-only hypothesis (B). The p value is the probability that $-2\ln Q < -2\ln Q_{\rm meas}$ in the B hypothesis. To compute the expected p value, we set $Q_{\rm meas}$ as the mode of the Q distribution assuming that σ' is equal to the theoretical prediction for the SM single top quark production cross section. To compare the data with the SM predictions, we then set σ' to be equal to $\sigma_{s+t}^{\rm meas}$ and compute the corresponding $Q_{\rm meas}$ and then the observed p value.

B. Constraining V_{tb}

We can also use the knowledge of the standard model prediction for the single top quark production cross section to compute the V_{tb} element of the Cabibbo-Kobayashi-Maskawa matrix. Under the standard model hypothesis, with the assumption that $|V_{td}|^2 + |V_{ts}|^2 \ll |V_{tb}|^2$ and that only $|V_{tb}|$ incorporates new physics contributions, one can measure V_{tb} using the relation $|V_{tb}|^2 = \sigma_{s+t}^{\rm meas}/\sigma_{s+t}^{\rm SM}$. The theoretical uncertainty on $\sigma_{s+t}^{\rm SM}$ is taken into account when setting the V_{tb} constraints, together with the uncertainty on the top quark pole mass measurement.

X. RESULTS

Using the signal and background modeling described in Sec. V, scanning the multivariate discriminant described in Sec. VII, and using the statistical test described above, we compute the probablility that the background (B) looks at least as signal-like as the data (observed p value) or as the median of signal plus background (S + B) pseudoexperiments outcomes (expected p value). Once including all systematic sources, we obtain an expected p value of 7.9×10^{-2} (1.4σ) and an observed p value of 1.6×10^{-2} (2.1σ). The distributions of $-2\ln Q$ for the B or S + B hypothesis are shown in Fig. 12, together with the observed outcome in the data.

Interpreting the 2.1σ excess as originating from single top quark production, we measure a single top quark production cross section of

$$\sigma_{s+t}^{\rm meas} = 4.9^{+2.5}_{-2.2}\ {\rm pb}.$$

The value measured in the data is compared to the measurement outcomes from 150 000 pseudoexperiments, as shown in Fig. 13. The single top quark production cross section measurement presented here is consistent with a $+1\sigma$ statistical upward fluctuation with respect to the standard model cross section. The probability to measure

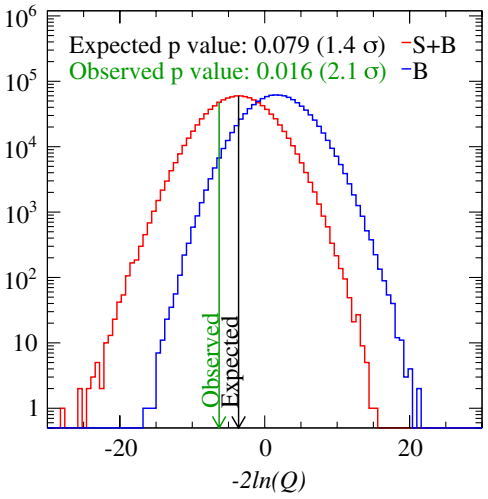

FIG. 12 (color online). Distribution of $-2\ln Q$ for the B or S + B hypothesis. The dark vertical arrow shows the mode of the $-2\ln Q$ distribution in the S + B hypothesis using pseudoexperiments, while the bright vertical arrow shows the outcome in data. The expected (observed) p value is the integral of the $-2\ln Q$ distribution in the B hypothesis at the left of the dark (bright) arrow.

a cross section higher than 4.9 pb has been estimated to be 18%.

As a cross-check, we perform the measurement separately in the three subsamples. The results are shown in Fig. 14 and indicate that, while the precision is low, the three orthogonal measurements are in agreement with each other.

Finally, we measure the V_{tb} element of the CKM matrix. Using an unconstrained flat prior on $|V_{tb}|^2$, we find $|V_{tb}| = 1.24^{+0.34}_{-0.29} \pm 0.07({\rm theory})$ as shown in Fig. 15(a). The theoretical uncertainty is due to the uncertainty on the standard

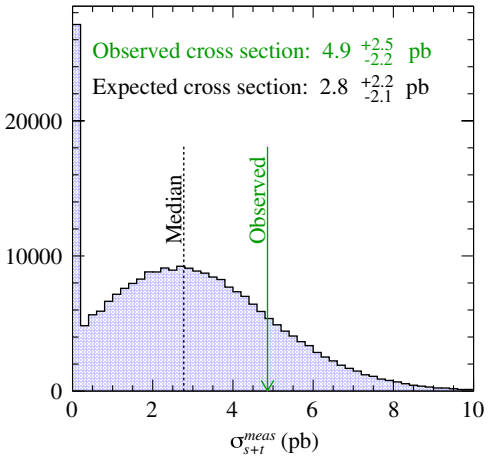

FIG. 13 (color online). Distribution of cross section measurement outcomes using pseudoexperiments. The green arrow shows the cross section measured in the data. The probability to measure a cross section higher than the median expected cross section shown as a dotted line is 18%.

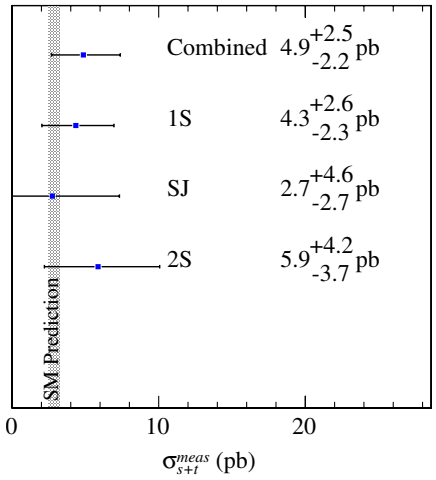

FIG. 14 (color online). Measurement of the single top quark cross section production. We show the combined result in the whole data set analyzed, and the result obtained in each tagging category. All measurements are consistent with the standard model theoretical cross section within uncertainties.

model theoretical cross section for single top quark production [6,7]. Assuming a flat prior on $|V_{tb}|^2$ between 0 and 1, Fig. 15 shows that $V_{tb} > 0.36$ at 95% credibility level.

The measurement presented here is consistent with a recent result from the D0 Collaboration analyzing 4.8 fb^{-1} of data, and requiring the explicit presence of an hadronic tau, $\not\!\!E_T$ and jets. The latter analysis observes a 1.9σ excess of single toplike events, and extracts a single top quark cross section $\sigma_{s+t} = 3.4^{+2.0}_{-1.8}$ pb [54].

XI. SUMMARY

We have presented the first search for s- and t-channel electroweak single top quark production in the $\not\!\!E_T$ + jets signature. This data set is orthogonal to the one used to achieve the evidence level at CDF [11] and D0 [9,10], and it is sensitive to the $W \to \tau\nu$ decays. Using an optimized neural network-based kinematic selection and b-jet identification techniques, we are able to improve the s/b of the initial sample obtained with a $\not\!\!E_T$ + jets trigger from about $1/10\,000$ to about $1/20$. We have analyzed 2.1 fb^{-1} of integrated luminosity recorded with the CDF II detector and observed an excess of signal-like events with respect to the standard model background prediction. The probability that the background-only hypothesis would produce the observed data is 1.6×10^{-2} (2.1σ). Assuming that the excess originates from single top quark production through s and t channels and a top quark mass of 175 GeV/c^2 we measure

$$\sigma^{\text{meas}}_{s+t} = 4.9^{+2.5}_{-2.2} \text{ pb}.$$

We use the theoretical computation of the signal cross section to measure the V_{tb} element of the CKM matrix:

$$|V_{tb}| = 1.24^{+0.34}_{-0.29} \pm 0.07(\text{theory}).$$

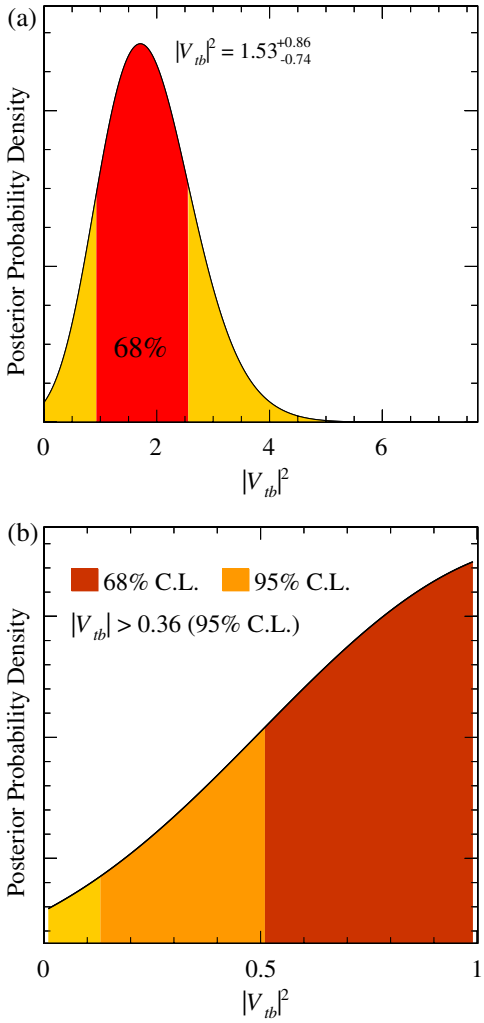

FIG. 15 (color online). Posterior probability density of the square of the V_{tb} element of the CKM matrix, assuming an unconstrained flat prior on V^2_{tb} (a) and assuming a flat prior on V^2_{tb} constrained between zero and one (b).

Assuming $0 \leq V_{tb} \leq 1$, we set the lower limit of $V_{tb} > 0.36$ at 95% confidence level. This analysis has been combined with the search performed by the CDF Collaboration in events with an identified charged lepton plus $\not\!\!E_T$ plus jets signature [13]. The combination of the two searches observes an excess of signal-like events over the background expectations at the 5σ level, thus establishing the existence of this rare process. Finally, the combination of the measurement presented here with the measurements in the charged lepton plus $\not\!\!E_T$ plus jets signatures by CDF and D0 has been performed to obtain the most precise direct measurement of V_{tb} to date [55].

ACKNOWLEDGMENTS

We thank the Fermilab staff and the technical staffs of the participating institutions for their vital contributions. This work was supported by the U.S. Department of

Energy and the National Science Foundation; the Italian Istituto Nazionale di Fisica Nucleare; the Ministry of Education, Culture, Sports, Science and Technology of Japan; the Natural Sciences and Engineering Research Council of Canada; the National Science Council of the Republic of China; the Swiss National Science Foundation; the A. P. Sloan Foundation; the Bundesministerium für Bildung und Forschung, Germany; the World Class University Program, the National Research Foundation of Korea; the Science and Technology Facilities Council and the Royal Society, UK; the Institut National de Physique Nucleaire et Physique des Particules/CNRS; the Russian Foundation for Basic Research; the Ministerio de Ciencia e Innovación, and Programa Consolider-Ingenio 2010, Spain; the Slovak R&D Agency; and the Academy of Finland.

[1] M. Cacciari, S. Frixione, M. L. Mangano, P. Nason, and G. Ridolfi, J. High Energy Phys. 04 (2004) 068; arXiv:hep-ph/0303085v1.
[2] N. Cabibbo, Phys. Rev. Lett. **10**, 531 (1963).
[3] M. Kobayashi and T. Maskawa, Prog. Theor. Phys. **49**, 652 (1973).
[4] J. Alwall *et al.*, Eur. Phys. J. C **49**, 791 (2007); arXiv:hep-ph/0607115.
[5] T. M. P. Tait and C. P. P. Yuan, Phys. Rev. D **63**, 014018 (2000).
[6] Z. Sullivan, Phys. Rev. D **70**, 114012 (2004).
[7] B. W. Harris *et al.*, Phys. Rev. D **66**, 054024 (2002).
[8] J. M. Campbell, R. Frederix, F. Maltoni, and F. Tramontano, Phys. Rev. Lett. **102**, 182003 (2009).
[9] V. M. Abazov *et al.* (D0 Collaboration), Phys. Rev. Lett. **98**, 181802 (2007); arXiv:hep-ex/0612052.
[10] V. M. Abazov *et al.* (D0 Collaboration), Phys. Rev. D **78**, 012005 (2008); arXiv:hep-ex/0803.0739.
[11] T. Aaltonen *et al.* (CDF Collaboration), Phys. Rev. Lett. **101**, 252001 (2008); arXiv:hep-ex/0809.2581.
[12] V. M. Abazov *et al.* (D0 Collaboration), Phys. Rev. Lett. **103**, 092001 (2009); arXiv:hep-ex/0903.0850.
[13] T. Aaltonen *et al.* (CDF Collaboration), Phys. Rev. Lett. **103**, 092002 (2009); arXiv:hep-ex/0903.0885.
[14] T. Aaltonen *et al.* (CDF Collaboration), arXiv:0911.3935.
[15] D. Acosta *et al.* (CDF Collaboration), Phys. Rev. D **71**, 032001 (2005).
[16] We use a cylindrical coordinate system where θ is the polar angle to the proton beam direction at the event vertex, ϕ is the azimuthal angle about the beam axis, and pseudorapidity is defined $\eta = -\ln\tan(\theta/2)$. We define transverse energy as $E_T = E\sin\theta$ and transverse momentum as $p_T = p\sin\theta$ where E is the energy measured in the calorimeter and p is the magnitude of the momentum measured by the spectrometer.
[17] C. S. Hill (CDF Collaboration), Nucl. Instrum. Methods Phys. Res., Sect. A **530**, 1 (2004).
[18] A. Sill (CDF Collaboration), Nucl. Instrum. Methods Phys. Res., Sect. A **447**, 1 (2000).
[19] A. A. Affolder *et al.* (CDF Collaboration), Nucl. Instrum. Methods Phys. Res., Sect. A **453**, 84 (2000).
[20] T. Affolder *et al.* (CDF Collaboration), Nucl. Instrum. Methods Phys. Res., Sect. A **526**, 249 (2004).
[21] L. Balka *et al.*, Nucl. Instrum. Methods Phys. Res., Sect. A **267**, 272 (1988).
[22] M. Albrow *et al.*, Nucl. Instrum. Methods Phys. Res., Sect. A **480**, 524 (2002).
[23] S. Bertolucci *et al.*, Nucl. Instrum. Methods Phys. Res., Sect. A **267**, 301 (1988).
[24] R. Blair *et al.*, Fermilab Report No. FERMILAB-PUB-96-390-E.
[25] G. Ascoli *et al.*, Nucl. Instrum. Methods Phys. Res., Sect. A **268**, 33 (1988).
[26] A. Abulencia *et al.* (CDF Collaboration), J. Phys. G **34**, 2457 (2007).
[27] F. Abe *et al.* (CDF Collaboration), Phys. Rev. Lett. **94**, 091803 (2005).
[28] A. Apresyan, Ph.D. thesis, Purdue University, 2009 [Fermilab Report No. FERMILAB-THESIS-2009-09].
[29] A. Bhatti *et al.*, Nucl. Instrum. Methods Phys. Res., Sect. A **566**, 375 (2006); arXiv:hep-ex/0510047.
[30] C. Adloff *et al.* (H1 Collaboration), Z. Phys. C **74**, 221 (1997).
[31] D. Acosta *et al.* (CDF Collaboration), Phys. Rev. D **71**, 052003 (2005).
[32] A. Abulencia *et al.* (CDF Collaboration), Phys. Rev. D **74**, 072006 (2006).
[33] J. Alwall *et al.*, J. High Energy Phys. 09 (2007) 028.
[34] H. L. Lai *et al.*, Eur. Phys. J. C **12**, 375 (2000); arXiv:hep-ph/9903282.
[35] T. Sjostrand *et al.*, Comput. Phys. Commun. **135**, 238 (2001).
[36] E. E. Boos *et al.*, Yad. Fiz. **69**, 1352 (2006) [Phys. At. Nucl. **69**, 1317 (2006)].
[37] V. N. Gribov *et al.*, Sov. J. Nucl. Phys. **15**, 438 (1972); G. Altarelli *et al.*, Nucl. Phys. **B126**, 298 (1977); Yu. L. Dokshitzer , Sov. Phys. JETP **46**, 641 (1977).
[38] J. Lueck, M.S. thesis, Karlsruhe University, 2009 [Fermilab Report No. FERMILAB-MASTERS-2006-01].
[39] A. Abulencia *et al.* (CDF Collaboration), J. Phys. G **34**, 2457 (2007); arXiv:hep-ex/0508029.
[40] A. Abulencia *et al.* (CDF Collaboration), Phys. Rev. D **74**, 032008 (2006); D. Acosta *et al.* (CDF Collaboration), Phys. Rev. Lett. **94**, 091803 (2005).
[41] J. M. Campbell and R. K. Ellis, Phys. Rev. D **62**, 114012 (2000).
[42] J. M. Campbell and R. K. Ellis, Phys. Rev. D **60**, 113006 (1999).
[43] K. Hornik *et al.*, *Multilayer Feedforward Networks Are Universal Approximators*, Neural Networks Vol. 2 (Elsevier Science, Oxford, UK, 1989), pp. 359–366; D. W. Ruck *et al.*, *The Multilayer Perceptron as an*

Approximation to a Bayes Optimal Discriminant Function, IEEE Transactions on Neural Networks Vol. 1 (IEEE, New York, 1990), No. 4, pp. 296–298.

[44] A. Hocker *et al.*, Proc. Sci. ACAT2007 (2007) 040; arXiv:physics/0703039.

[45] R. Brun and F. Rademakers, Nucl. Instrum. Methods Phys. Res., Sect. A **389**, 81 (1997).

[46] A momentum tensor is defined as $M_{lm} = \sum_o j_l^o j_m^o / \sum_o |\vec{j}^o|$, where $\vec{j}^o$ is the momentum of a reconstructed jet, and l and m are Cartesian coordinates. The index o runs over the number of jets in the event. The sphericity in an event is defined as $S = \frac{3}{2}(\lambda_2 + \lambda_3)$, where λ_2 and λ_3 are the smallest two eigenvalues of the normalized momentum tensor.

[47] D. Acosta *et al.*, Nucl. Instrum. Methods Phys. Res., Sect. A **494**, 57 (2002).

[48] T. Sjostrand, Phys. Lett. **157B**, 321 (1985); M. Bengtsson *et al.*, Z. Phys. C **32**, 67 (1986).

[49] A. D. Martin, R. G. Roberts, W. J. Stirling, and R. S. Thorne, Eur. Phys. J. C **4**, 463 (1998); arXiv:hep-ph/9803445.

[50] J. Pumplin, D. R. Stump, J. Huston, H. L. Lai, P. M. Nadolsky, and W. K. Tung, J. High Energy Phys. 07 (2002) 012; arXiv:hep-ph/0201195.

[51] Tevatron Electroweak Working Group, CDF and D0 Collaborations, arXiv:hep-ex/0903.2503.

[52] C. Amsler *et al.* (Particle Data Group), Phys. Lett. B **667**, 1 (2008).

[53] J. Neyman and E. Pearson, Phil. Trans. R. Soc. A **231**, 289 (1933).

[54] V. M. Abazov *et al.* (D0 Collaboration), arXiv:hep-ex/0912.1066.

[55] Tevatron Electroweak Working Group, CDF and D0 Collaboration, arXiv:hep-ex/0908.2171.